Organization of the apical extracellular matrix during tubular organ formation

J. Luke Woodward[1,¶], Jeffrey Matthew[1,¶], Rutuparna Joshi[1], Vishakha Vishwakarma[1], Ying Xiao[2], and SeYeon Chung[1,*]

1 Department of Biological Sciences, Louisiana State University, Baton Rouge, LA 70803, USA

2 Shared Instrumentation Facility, Louisiana State University, Baton Rouge, LA 70803, USA

¶ These authors contributed equally to this study.

*Author for correspondence: seyeonchung@lsu.edu

Abstract

The apical extracellular matrix (aECM) plays a critical role in epithelial tube morphogenesis during organ formation, but its composition and organization remain poorly understood. Using the *Drosophila* embryonic salivary gland (SG) as a model, we identify Papss, an enzyme that synthesizes the universal sulfate donor PAPS, as a critical regulator of tube lumen expansion. *Papss* mutants show a disorganized apical membrane, condensed aECM, and disruptions in Golgi structures and intracellular trafficking. SG-specific expression of wild-type Papss, but not the catalytically inactive form, rescues the defects in *Papss* mutants, suggesting that defects in sulfation are the underlying cause of the phenotypes. Additionally, we identify two zona pellucida (ZP) domain proteins, Piopio (Pio) and Dumpy (Dpy), as key components of the SG aECM. In the absence of *Papss*, Pio is gradually lost in the aECM, while the Dpy-positive aECM structure is condensed and dissociates from the apical membrane, leading to a thin lumen. Mutations in *dpy* or *pio*, or in *Notopleural*, which encodes a matriptase that cleaves Pio to form the luminal Pio pool, result in a SG lumen with alternating bulges and constrictions, with the loss of *pio* leading to the loss of Dpy in the lumen. Our findings underscore the essential role of sulfation in organizing the aECM during tubular organ formation and highlight the mechanical support provided by ZP domain proteins in maintaining luminal diameter.

Introduction

Epithelial tubes are critical components of many key biological organs, including the kidney, heart, and lungs. Aberrant tube size leads to common diseases and congenital disorders, such as polycystic kidney disease, asthma, and lung hypoplasia. Tube morphogenesis is regulated by multiple factors, including intracellular mechanisms, intercellular interactions, and interactions between cells and the surrounding extracellular matrix (ECM). Specifically, events at the apical (luminal) surface of a tube play an important role in regulating tube diameter and growth, thereby influencing overall tube shape (Myat and Andrew, 2002). During tubular organ formation, the surrounding epithelium secretes apical ECM (aECM) components into the lumen. These aECM components form the luminal meshwork and interact with the apical membrane, playing a critical role in epithelial morphogenesis and regulation of tube dimensions (Jazwinska et al., 2003; Devine et al., 2005; Luschnig et al., 2006; Wang et al., 2006; Syed et al., 2012; Dong et al., 2014; Drees et al., 2023; Gill et al., 2016; Cohen, Sparacio, et al., 2020).

The aECM has a distinct composition compared to the basal ECM, with a diverse array of components (Zheng et al., 2020). ZP domain proteins, which are highly conserved across species, are of particular interest and are characterized by a conserved 260 amino acid ZP domain that mediates homo- or heteromeric polymerization into filaments. Initially identified in the extracellular coat of mammalian oocytes, ZP domain proteins have been shown to play a critical role in the organization of specialized apical structures in various tissues in species ranging from worms to humans (Porter & Tamm, 1955; Yan et al., 2012; Legan et al., 1997; Op De Beeck et al., 2012; Renner et al., 2007; McAllister et al., 1994; Wong et al., 2000; Cohen, Bermudez, et al., 2020; Plaza et al., 2010; Jovine et al., 2005; Litscher & Wassarman, 2020; Wilkin et al., 2000; Ghosh & Treisman, 2024). Chitin, a biopolymer of N-acetylglucosamine, is another major aECM component that is abundant in invertebrates and some vertebrates (Tang et al., 2015; Mei et al., 2024). In many *Drosophila* and *C. elegans* tissues, chitin forms a network of fibers that provide mechanical support and maintain the integrity of the epithelial layer (Araujo et al., 2005; Devine et al., 2005; Moussian et al., 2006; Tonning et al., 2005; Zhang et al., 2005). Several studies have shown the role of ZP proteins in maintaining the chitin matrix in the aECM. During *Drosophila* tracheal development, two ZP proteins, Dumpy (Dpy) and Piopio (Pio), build an elastic structure in the lumen that modulates mechanical stress and maintains the chitin matrix

62 (Jazwinska et al., 2003; Dong et al., 2014; Drees et al., 2023). In the *Drosophila* corneal lens,
63 another ZP domain protein, Dusky-like, establishes an external scaffold for chitin retention
64 (Ghosh & Treisman, 2024). However, many organs in both vertebrates and invertebrates have a
65 non-chitinous aECM, and the role of ZP proteins in the non-chitinous aECM is less well
66 understood.

67 Post-translational modifications of the aECM are essential for proper tube dimensions
68 during organ formation (Luschnig et al., 2006; Wang et al., 2006; Abrams et al., 2006; Herman
69 & Horvitz, 1999; Hwang et al., 2003). Sulfation is an abundant post-translational modification
70 that takes place in the Golgi apparatus, where a sulfate group is covalently attached to amino
71 acid residues of proteins or side chains of proteoglycans (Gunal et al., 2019). Several studies in
72 *C. elegans* have shown key roles of sulfation in neuronal organization, development of
73 reproductive tissues, and phynotypic plasticitiy, linking this post-translational modification to
74 multiple cellular processes (Turnbull et al., 2003; Bulow & Hobert, 2004; Kinnunen et al., 2005;
75 Tecle et al., 2013; Diaz-Balzac et al., 2014; Dierker et al., 2016). A study in a mouse model of
76 cystic fibrosis also suggest a link between the disease state and proper sulfation levels in organs
77 (Xia et al., 2005), but the role of sulfation in tubular organ development and aECM organization
78 remains elusive.

79 Sulfation reactions require a high-energy form of sulfate, 3'-phosphoadenosine-5'-
80 phosphosulfate (PAPS), which is produced by the enzyme PAPS synthetase (Papss) (van den
81 Boom et al., 2012; Gunal et al., 2019). Mammals have two Papss isoforms, Papss1 and Papss2.
82 *Papss1* shows ubiquitous expression, with higher levels in glandular cells and salivary duct cells,
83 suggesting that high degrees of sulfation are required in these cell types (Uhlen et al., 2005;
84 Karlsson et al., 2021). *Papss2* shows a more restricted expression in certain tissues such as
85 cartilage, and mutations in *Papss2* have been associated with skeletal dysplasia in humans
86 (Faiyaz ul Haque et al., 1998; Ahmad et al., 1998; Kurima et al., 1998; Ford-Hutchinson et al.,
87 2005). Mouse models with exon deletions in *Papss1* or *Papss2* show extensive defects, including
88 lethality (*Papss1*) and abnormal craniofacial and limb morphology (*Papss2*) (Groza et al., 2023),
89 demonstrating that Papss is vital for developmental processes in mammals. *Drosophila* has a
90 single *Papss* gene, allowing for a straightforward investigation of its function in developmental
91 processes without redundancy. By studying the role of *Papss* in *Drosophila* development, we can

92 gain valuable insights into the role of this conserved enzyme in normal development and disease
93 in humans.

94 To understand the role of post-translational modification in aECM organization and to
95 determine the key composition of the non-chitinous aECM in tubular organs, we use the
96 *Drosophila* embryonic SG as a model. This single-layered epithelial tube is formed through
97 highly stereotyped morphogenetic processes (Chung et al., 2014), making it an excellent system
98 for elucidating the molecular mechanisms underlying aECM composition and modification. SG
99 cells are specified on the ventral surface of the embryo at stage 10. Once specified, SG cells do
100 not undergo cell division or cell death because SG-upregulated transcription factors
101 downregulate the expression of key cell cycle genes and proapoptotic genes (Myat & Andrew,
102 2000a; Chandrasekaran & Beckendorf, 2003; Fox et al., 2013; Matthew et al., 2024), and thus
103 the entire morphogenetic process is driven by cell shape change, cell rearrangement, and
104 collective cell migration (Myat & Andrew, 2000b; Bradley & Andrew, 2001; Bradley et al.,
105 2003; Chung & Andrew, 2014; Chung et al., 2017). At stage 11, SG cells invaginate to form a
106 three-dimensional tubular structure, which then elongates and migrates toward its final position
107 during stages 12-13. The SG continues to migrate and the lumen expands significantly by apical
108 secretion during stages 14-16, forming the fully developed organ. Despite limited knowledge of
109 the composition of the aECM in the SG, previous work has demonstrated the critical role of
110 ADAMTS-A, a secreted metalloprotease, in releasing cells from the aECM to facilitate SG
111 migration and normal lumen shape (Ismat et al., 2013). Our previous work has also shown that
112 cell-aECM adhesion via the apical surface protein Cad99C influences cell rearrangement during
113 SG elongation (Chung & Andrew, 2014).

114 Here, we identify Papss as being essential for aECM organization and lumen expansion
115 of the *Drosophila* embryonic SG. Loss of *Papss* results in a disorganized apical membrane and a
116 condensed aECM, which is associated with disrupted Golgi structures and intracellular
117 trafficking. *Papss* mutants also show defects in the basal ECM and occasional SG cell death,
118 leading to invasion of hemocytes into SG epithelia that engulf dying cells. Expressing the wild-
119 type (WT) Papss in the SG rescues all phenotypes, but not the enzyme-dead form. We identify
120 two ZP proteins, Pio and Dpy, as key components of the SG aECM. In the SG lumen, these ZP
121 domain proteins form a filamentous scaffold that is significantly affected by the loss of *Papss*,

122 with Pio eventually being lost from the aECM and the Dpy-positive aECM structure condensing
123 and dissociating from the apical membrane. Mutations in *pio* or *dpy*, or in *Notopleural* (*Np*),
124 which encodes a matriptase that cleaves Pio to form the luminal pool of Pio, exhibit bulging and
125 constriction of the SG lumen. Notably, mutations in *pio* result in the loss of luminal Dpy signals
126 in the SG. These data indicate that the Dpy-containing filamentous structure of the aECM is
127 crucial for maintaining luminal diameter and that the luminal pool of Pio is essential for
128 organizing this structure during SG morphogenesis.

Results

Papss is required for SG lumen expansion

To identify key enzymes that affect SG morphology by modifying aECM components, we examined the effects of the loss of ~20 enzymes that are highly expressed in the SG and are likely to function in the secretory pathway (Fox et al., 2013). Deficiency lines deleting each enzyme were immunostained with the apical membrane marker Crumbs (Crb) or Stranded at Second (SAS) to assess SG lumen shape. Among the twelve lines showing defects (Table 1), a deficiency line deleting *PAPS synthetase* (*Papss*) and 18 other genes had a very thin SG lumen with irregular apical protrusions (Figure 1A). Papss catalyzes the synthesis of 3'-phosphoadenosine-5'-phosphosulfate (PAPS), the sulfate donor compound in all sulfotransferase reactions (Venkatachalam, 2003). Consistent with a previous report (Jullien et al., 1997), our fluorescence in situ hybridization confirmed that *Papss* transcripts are highly expressed in the SG throughout morphogenesis (Figure 1B), suggesting a high demand for sulfation in this organ.

To test the role of *Papss* and confirm the phenotype, we used a *Papss* EMS mutant line (*Papss*^{2}; Zhu et al., 2005). The Papss protein contains two critical protein domains, the ATP sulfurylase domain, which adds sulfate to an AMP group of ATP to form adenosine 5'-phosphosulfate (APS), and the APS kinase domain, which phosphorylates APS to form PAPS (Venkatachalam et al., 1998; Mueller & Shafqat, 2013). Sanger sequencing of this mutant identified a point mutation (G->A) that introduces a premature stop codon (Trp271->stop; amino acid number is for the Papss-PA isoform) located near the N-terminus of the ATP sulfurylase domain, resulting in a truncated protein in which most of the domain is not translated (Figure 1-figure supplement S1A-B). Since both protein domains are essential for the enzyme function of Papss, we conclude that this mutant line is potentially null or a strong hypomorphic allele. *Papss* homozygous mutants and transheterozygotes for *Papss* mutant over a deficiency were embryonic lethal. To test the role of Papss in sulfation in the SG, we checked for the presence of sulfated tyrosine using a sulfotyrosine antibody in WT and *Papss* mutant embryos. In WT, we observed strong sulfotyrosine signals both in the apical membrane and as puncta in the cytoplasm of SG cells (Figure 1-figure supplement S2A). The cytoplasmic puncta colocalized with ManII-GFP signals, a medial Golgi marker (Yang et al., 2021), suggesting that proteins undergoing tyrosine sulfation in the Golgi are detected by the antibody (Figure 1-figure supplement S2C). In *Papss*

159 mutants, the cytoplasmic punctate signals were significantly reduced (Figure 1-figure
160 supplement 2B), suggesting that sulfation in the Golgi is decreased. The signals at the apical
161 membrane appeared similar or slightly reduced compared to WT, suggesting that sulfated
162 molecules, possibly by maternally provided Papss, were still targeted apically, although it is not
163 clear whether they were properly targeted to their original destination or mislocalized. Together
164 with a previous study using Alcian Blue staining showing the loss of sulfated biomolecules in the
165 *Papss* mutant SG (Zhu et al., 2005), these data suggest sulfation in the SG is dependent on Papss.

166 *Papss* homozygous mutant embryos often showed overall defective embryonic
167 morphology, such as defects in germ band retraction and head involution (39%; N=80/204;
168 Figure 1-figure supplement 3A-F). The heterozygous *Papss* mutant embryos produced by
169 crossing *Papss* mutants with WT flies appeared normal (Figure 1-figure supplement 3A-F). A
170 smaller percentage of transheterozygous embryos showed similar defects (10%; N=13/136), with
171 many late-stage embryos appearing normal (Figure 1-figure supplement 3C, E and F). We
172 conclude that transheterozygous embryos with more severe defects did not survive to late stages,
173 but we cannot rule out the possibility that a secondary mutation at another gene locus contributes
174 to the overall embryonic defects. Embryos with these morphological defects often showed
175 defects in SG invagination, forming a SG close to the surface of the embryo (Figure 1-figure
176 supplement 3D, G and H). We used the embryos that formed the SG in the normal position for
177 quantification and further analysis.

178 Using the adherens junction (AJ) marker E-cadherin (Ecad) signals, we analyzed SG
179 lumen phenotypes in *Papss* homozygous mutant embryos and transheterozygotes. During stages
180 14-16, the WT SG lumen expanded consistently throughout its length (Figure 1C). In contrast,
181 *Papss* mutant embryos exhibited irregularities in SG lumen expansion. At stage 14, when the
182 WT SG lumen expansion began, more than 40% of *Papss* mutant embryos had either a thinner
183 lumen (Figure 1D and I; 18%; N=7/38) or a slightly irregular lumen with bulges (Figure 1D and
184 I; 24%; N=9/38). At stage 16, about half of *Papss* homozygous or mutant embryos or
185 transheterozygotes over a deficiency showed an overall thin lumen with an irregular apical
186 surface (Figure 1D and I') and the other half had an irregularly expanded lumen with thin and
187 expanded regions along its length (Figure 1D and I'). Quantification of the SG lumen length and
188 diameter at stage 16 showed that whereas the lumen length was comparable between WT and

189 *Papss* mutant SGs (Figure 1J), the diameter was significantly decreased or irregular, with a high
190 degree of variation in *Papss* mutant SGs (Figure 1K and K'). Quantification of the SG lumen
191 area at stage 16 revealed that *Papss* mutants SGs exhibiting the thin lumen phenotype had a
192 smaller lumen size compared to WT. Together, these data suggest a role for Papss in SG lumen
193 expansion primarily by expanding the lumen diameter (Figure 1L).

194 To determine whether the SG lumen expansion defects are due to the loss of *Papss*, we
195 performed a rescue experiment by overexpressing Papss in the SG using the SG-specific driver
196 *sage-Gal4* (Chung et al., 2009) in the *Papss* mutant background. *Papss* produces multiple
197 isoforms, including Papss-PA/B/C/G (629 aa), Papss-PD (657 aa), and Papss-PE/F/H (630 aa),
198 which differ only slightly in the N-terminus (Flybase; www.flybase.org). Using three additional
199 probes that detect different subsets of splice forms, we performed fluorescent in situ
200 hybridization and found that all probes detected signals in the SG at varying levels (Figure 1-
201 figure supplement 4A and B). We generated UAS lines for Papss-PD and Papss-PE and found
202 that overexpression of either isoform in the SG of WT embryos resulted in a normally expanded
203 SG lumen (data for Papss-PE overexpression are shown in Figure 1F and I'). Given the high
204 levels of *Papss* mRNA in the WT SG, the Papss protein is likely abundant in the SG, which may
205 explain why further overexpression of Papss does not lead to any additional effects. Since our
206 initial analysis showed identical rescue features in the SG for the generated UAS lines, we used
207 the UAS-Papss-PD and UAS-Papss-PE lines interchangeably for further experiments (hereafter,
208 when overexpressed, Papss-PD and Papss-PE will be referred to as Papss). When Papss was
209 overexpressed in the SG of *Papss* mutant embryos, only a small fraction (4%; N=1/26) showed a
210 thin lumen phenotype along the entire length of the SG (Figure 1G and I'). The majority of
211 embryos (73%) showed either a normal, fully expanded lumen along the entire length of the SG,
212 with occasional slight irregularities at the apical membrane (42%; N=11/26), or a irregularly
213 expanded lumen, where some parts of the SG lumen were expanded and others were thin (31%;
214 N=8/26) (Figure 1G and I'). SGs with normally expanded lumens had luminal geometry
215 comparable to that of WT embryos (Figure 1J-L). Interestingly, some of the embryos had an
216 over-expanded SG lumen, often with a non-uniform diameter (24%; N=6/24; Figure 1G and I').
217 To test whether the enzyme activity of Papss is required for its role in SG lumen expansion, we
218 also generated UAS lines with mutations in the critical residues of the ATP sulfurylase (F593P)
219 and APS kinase (K193A) domains using the Papss-PD isoform (See Materials and Methods for

220 details; amino acid number is for Papss-PD). Overexpressing a mutant version of Papss
221 containing both of these mutations in the SG did not rescue the SG phenotypes as WT Papss did,
222 but it showed the same range of defects as *Papss* mutants (Figure 1H, I' and J-L). These data
223 suggest that the sulfation activity of Papss is required for SG lumen expansion. Overall, although
224 a range of phenotypes was present, the thin SG lumen phenotype was almost completely rescued
225 by SG-specific expression of WT Papss, but not the enzyme-dead form.

226

227 **Loss of *Papss* disrupts the apical domain and aECM organization**

228 To investigate the cellular basis of the thin SG lumen phenotype in *Papss* mutants, we examined
229 the localization of key apical membrane proteins and junctional markers. In WT SGs, the apical
230 polarity protein Crb localized to the subapical region (SAR) between the apical surface (free
231 apical area) and the AJs, and we observed clear Crb signals along the apical cell boundary of
232 each SG cell (Figure 2A and B). In contrast, the Crb signals in *Papss* mutants appeared less
233 prominently localized to the SAR in SG cells (Figure 2C). We measured the Crb signal intensity
234 in the SAR and the apical-medial region of SG cells. The ratio of the Crb signal intensity at SAR
235 to apical-medial intensity was significantly lower in *Papss* mutants than in WT (Figure 2D),
236 indicating disorganization of the apical domain. The AJ marker Ecad and the septate junction
237 (SJ) marker Discs large (Dlg) showed no apparent disruption in localization compared to WT
238 (Figure 2-figure supplement 1A-E). These data suggest that loss of *Papss* primarily affects the
239 apical membrane in the SG, while leaving the junctional regions intact.

240 Next, we investigated the organization of the aECM, using wheat germ agglutinin (WGA),
241 which marks several glycan modifications including O-linked β-N-acetylglucosamine (O-
242 GlcNAc). WGA has been shown to label the apical membrane and luminal structure in the
243 *Drosophila* embryonic trachea (Tonning et al., 2005; Chung et al., 2009). Similarly, we observed
244 relatively weak WGA signals in the apical membrane and the lumen of WT SGs (Figure 2E; n=25
245 SGs). Notably, the luminal signals showed multiple thin filamentous organizations traversing the
246 lumen (Figure 2E), suggesting heterogeneity of the luminal structure. In *Papss* mutants, WGA
247 signals were increased in both the lumen and apical membrane, with the apical membrane signals
248 appearing more diffuse (Figure 2F; n=28 SGs). Interestingly, the luminal WGA signals in *Papss*

249 mutants accumulated strongly on one side along the entire length of the lumen, whereas the thin
250 filamentous WGA signals in WT SGs appeared to show no bias and were mostly centered in the
251 lumen. In regions with a thin SG lumen, WGA was present in a highly condensed rod-like
252 structure; in expanded regions, WGA signals showed either a similar condensed rod-like structure
253 favoring one side of the SG lumen or a slightly condensed filamentous structure often broadly
254 associated with the apical membrane (Figure 2F). Transmission electron microscopy (TEM)
255 analysis also revealed highly condensed and more electron-dense luminal structures in the SG of
256 *Papss* mutants compared to WT (Figure 2H and I; original, raw TEM images of several WT and
257 *Papss* mutant samples are shown in Figure 2-figure supplement 2A and B). SG-specific
258 overexpression of Papss in the *Papss* mutant background resulted in a partial rescue; the luminal
259 WGA structures were less condensed than *Papss* mutants, but they were not as thin as those in WT
260 SGs (Figure 2G). Taken together, these data suggest a role for Papss in organizing the SG aECM
261 with loss of *Papss* resulting in a tightly packed or condensed aECM that is loosely associated with
262 the apical membrane.

263

264 **Loss of *Papss* disrupts Golgi organization and mislocalizes intracellular trafficking**
265 **markers**

266 In addition to the apical membrane and luminal signals, we detected WGA signals around the
267 nucleus, consistent with WGA binding to glycoproteins on the nuclear envelope (Rutherford et al.,
268 1997), and in several large, punctate cytoplasmic structures in WT SG cells (Figure 3A and E).
269 The cytoplasmic WGA puncta colocalized with the medial-Golgi marker ManII-GFP, suggesting
270 that WGA binds glycoproteins in the Golgi (Figure 3J and L). The number and intensity of the
271 punctate WGA signals were significantly reduced in *Papss* mutants (Figure 3B, F, I and I').
272 Overexpression of WT Papss, but not the mutant form of Papss, in the SG restored the number of
273 WGA cytoplasmic puncta (Figure 3C, D, G, H, I and I'). The intensity of the WGA signals was
274 not restored in either case (Figure 3I').

275 Interestingly, we observed highly dispersed ManII-GFP signals in *Papss* mutants SGs
276 (Figure 3K and L'), suggesting that Golgi structures may be disrupted upon *Papss* loss. To examine
277 the Golgi structures in more detail, we performed TEM analysis in WT and *Papss* mutant SG cells.

278 In contrast to the mammalian Golgi, the *Drosophila* Golgi lacks the characteristic ribbon-like
279 structure and is composed of a series of individual cisternae arranged in a random, disordered
280 fashion (Kondylis & Rabouille, 2009). While the Golgi in WT SG cells showed randomly arranged
281 cisternae, the Golgi in *Papss* mutants showed abnormal arrangement, either stacked or
282 compressed, with small electron-dense puncta along these structures (Figure 3M and N),
283 suggesting a functional defect and possible protein aggregation. Other organelles, such as the
284 endoplasmic reticulum (ER), appeared relatively normal. SG-specific expression of GFP-KDEL,
285 GFP fused to the ER retention motif KDEL, or immunostaining for prolyl-4-hydroxylase-alpha
286 SG1, an ER-resident enzyme (Abrams et al., 2006), showed no significant differences between
287 WT and *Papss* mutant SGs (Figure 3-figure supplement 1 A-D). TEM analysis also revealed
288 similar ER structures in WT and *Papss* mutant SG cells (Figure 3-figure supplement 1E and F).
289 These data suggest that loss of *Papss* disrupts the Golgi, but not the ER.

290 To determine whether the phenotypes observed in *Papss* mutants are due to defects in
291 Golgi structure and function, we examined the morphology of the SG in null mutants of two key
292 Golgi components, GM130 and Grasp65 (Zhou et al., 2014). Both mutants were homozygous-
293 viable. Although the GM130 null allele ($GM130^{\Delta 23}$) was extremely weak and difficult to grow, the
294 embryos we managed to collect appeared normal, and the SG exhibited only mild irregularity
295 (Figure 3-figure supplement 2A; n=5/5). It is possible that only relatively normal embryos survived
296 until late stages of embryogenesis. However, *Grasp65* null mutants ($Grasp65^{102}$) exhibited a
297 highly irregular SG lumen with condensed luminal WGA signals (Figure 3-figure supplement 2B
298 and C; n=10/10). These data suggest that disrupted Golgi structures in *Papss* mutants may
299 contribute to the SG defects.

300 The aberrant Golgi structures observed in *Papss* mutants prompted us to investigate the
301 impact on intracellular trafficking components. We examined the localization of Rab11, a marker
302 for recycling endosomes, Rab7, a marker for late endosomes, and Sec15, an exocyst marker. As
303 previously shown (Chung & Andrew, 2014; Le & Chung, 2021), Rab11 and Sec15 were enriched
304 along the apical domain of WT SG cells (Figure 3O and Q). In *Papss* mutants SGs, we observed
305 an increase in apical Rab11 signal intensity, with some signals mislocalized to the basolateral
306 region (Figure 3P and S). In contrast, Sec15 signals were significantly reduced at the apical
307 membrane (Figure 3R and T). Unlike Rab11 or Sec15, Rab7 localized in large punctate structures

308 in the cytoplasm of WT SG cells (Figure 3-figure supplement 3A). In *Papss* mutants, the number
309 of Rab7 puncta was significantly reduced, although the intensity of Rab7 puncta was not
310 significantly different from WT (Figure 3-figure supplement 3B-D). TEM analysis revealed a
311 number of electron-dense vesicles in the apical domain of SG cells in WT (Figure 3U). In contrast,
312 *Papss* mutant SGs showed fewer electron-dense vesicles, but instead we observed several larger,
313 empty vesicle-like structures (Figure 3V and W). Collectively, these data suggest that defective
314 sulfation affects Golgi structures and multiple routes of intracellular trafficking.

315

316 **Loss of *Papss* results in abnormal cell death and disruption of the basal ECM**

317 In *Papss* mutant embryos, we often observed one or more acellular regions within the SG
318 epithelium during late embryogenesis that lacked any markers for nuclei, cell membranes, or
319 junctions. To test whether these acellular regions were caused by cell death, we stained embryos
320 with an antibody against *Drosophila* cleaved death caspase-1 (DCP-1; Sarkissian et al., 2014).
321 Indeed, DCP-1 signals were often found within the acellular spaces (Figure 4A and B),
322 suggesting that loss of *Papss* leads to abnormal cell death in the SG. TEM analysis also captured
323 a dying cell in the *Papss* mutant SG supporting the occurrence of cell death (Figure 4C). We
324 found that *Papss* mutant SGs have a significantly higher number of these acellular spaces
325 compared to WT SGs (Figure 4D). Quantifying the number of SG cells at stage 16 revealed that
326 *Papss* homozygous embryos and transheterozygotes have significantly fewer cells than WT
327 (Figure 4E). Overexpression of WT Papss, but not the mutant form of Papss, in the *Papss* mutant
328 background decreased the number of acellular regions within the SG (Figure 4D) and restored
329 the number of SG cells (Figure 4E). This suggests that loss of sulfation leads to conditions that
330 hinder SG cell survival. Blocking apoptosis in the *Papss* mutant SG by overexpressing the
331 baculoviral protein p35, a caspase inhibitor of apoptosis, also restored the SG cell number
332 (Figure 4E), suggesting that apoptosis is a key mechanism underlying SG cell loss in *Papss*
333 mutants. Importantly, the SGs in these embryos still showed thin (25%; N=2/8) or irregularly
334 expanded (75%; N=6/8) lumens, suggesting that SG lumen expansion defects in *Papss* mutants
335 are independent of abnormal cell death.

336 Using srpHemo3x-mCh (Gyoergy et al., 2018), we labeled hemocytes, which are
337 analogous in function to macrophages in vertebrates. Hemocyte signals were often present in the
338 acellular regions of the SG in *Papss* mutants, suggesting that hemocytes may aid in apoptotic cell
339 clearance from the SG epithelium (Figure 4F and G). In normal epithelia, the basal ECM acts as
340 a physical barrier, preventing hemocytes from migrating into the epithelial layer. To examine the
341 integrity of the basal ECM in *Papss* we used an antibody against Nidogen (Ndg), a glycoprotein
342 with important linker functions in the basement membrane (Wolfstetter & Holz, 2012). Ndg-
343 positive basal ECM was detected in a regular, thin layer around WT SGs at stage 16 (Figure 4H).
344 However, in *Papss* mutants, Ndg signals were irregular and often disconnected, and hemocytes
345 invaded SG cells through the gaps in the Ndg-positive basal ECM (Figure 4I). Overall, our data
346 suggest that loss of *Papss* leads to aberrant cell death in the SG and disrupts both the apical and
347 basal ECM of the SG.

348

349 **The ZP domain proteins Pio and Dpy of the SG aECM are affected by the loss of *Papss***

350 To better understand how aECM composition and organization are affected by *Papss* loss, we set
351 out to identify SG aECM components. Since chitin, a major aECM component in many *Drosophila*
352 tissues, is absent from the SG lumen (Figure 5A), we focused on ZP domain proteins. Of the 18
353 ZP domain proteins in *Drosophila*, at least six are expressed in the embryonic SG, including *pio*,
354 *dpy*, *quasimodo* (*qsm*), *cypher* (*cyr*), *dusky* (*dy*), and *CG17111* (Tomancak et al., 2002; Jazwinska
355 & Affolter, 2004; Weiszmann et al., 2009). We assessed the localization of Pio and Dpy, key
356 aECM components critical for *Drosophila* tracheal morphogenesis (Jazwinska et al., 2003; Drees
357 et al., 2023), and Qsm, which plays a critical role in remodeling Dpy in the aECM during
358 *Drosophila* flight muscle development (Chu & Hayashi, 2021).

359 To test Pio localization in the SG, we used a transgenic line expressing an mCherry-Pio
360 (mCh-Pio) fusion protein with the N-terminal mCh tag (Drees et al., 2023; Figure 5B), as well as
361 a Pio antibody generated with the peptide corresponding to the sequence within the ZP domain of
362 Pio, between the ZP-N and ZP-C domains (Jazwinska et al., 2003; Figure 5B). mCh-Pio signals
363 were observed in cytoplasmic puncta, at the apical membrane, and in the SG lumen. These signals,
364 especially the luminal signals, became stronger at stages 15-16 (Figure 5C), suggesting that Pio is

365 transported apically and secreted into the SG lumen. Pio antibody signals showed distinct
366 localization, predominantly in the SG lumen and at the apical membrane (Figure 5E and F). At
367 stages 11 and 12, the Pio antibody revealed low levels of cytoplasmic punctate signals along with
368 strong luminal signals, but from stage 13, Pio signals were predominantly localized to the SG
369 lumen (Figure 5E and F; Figure 5-figure supplement 1A). Interestingly, compared to the diffuse
370 luminal mCh-Pio signals (Figure 5C), Pio antibody signals in the SG lumen were heterogeneous
371 with filamentous structures (Figure 5E-6F''), resembling luminal WGA signals. Pio antibody
372 signals were absent at all stages in the *pio* null mutant, in which the entire ZP domain is deleted
373 (Drees et al., 2023; Figure 5-figure supplement 1B and C), confirming antibody specificity. The
374 Pio protein is known to be cleaved, at one cleavage site after the ZP domain by the furin protease
375 and at another cleavage site within the ZP domain by the matriptase Notopleural (Np) (Drees et
376 al., 2019; Drees et al., 2023; Figure 5B). The latter cleavage site falls within the peptide sequence
377 used to generate the Pio antibody (Figure 5B). A possible explanation for the different signals
378 between mCh-Pio and Pio antibody signals is that the Pio antibody preferentially recognizes the
379 C-terminal ZP domain fragment after furin and Np cleavage, whereas diffuse, luminal mCh-Pio
380 signals are either the secreted Pio protein cleaved only by furin or the N-terminal fragment after
381 Np cleavage.

382 Dpy-YFP signals from the Dpy-YFP knock-in line (Lye et al., 2014; YFP insertion into the
383 *dpy* locus near the middle of the protein) showed heterogeneous, filamentous structures in the SG
384 lumen throughout SG morphogenesis (Figure 5-figure supplement 2A) that colocalized with Pio
385 antibody and WGA signals (Figure 5E-F"; Figure 5-figure supplement 2C). It should be noted that
386 because homozygous Dpy-YFP embryos showed a bulging and constricted SG lumen phenotype
387 with highly condensed Dpy-YFP signals throughout the lumen (Figure 5-figure supplement 2B),
388 we used embryos with one copy of the transgene to analyze Dpy localization. Qsm localization
389 was analyzed using the mCh-Qsm knock-in line, in which mCh is inserted into the *qsm* locus a
390 few amino acids downstream of the N-terminal end of the protein (Chu & Hayashi, 2021). Unlike
391 Pio and Dpy, mCh-Qsm signals were not detected in the SG lumen. Instead, they showed a
392 dynamic intracellular localization ranging from cytoplasmic signals with apical membrane
393 enrichment (stages 11-14) and apical vesicular signals (stages 14-15) to prominent signals at the
394 apical membrane and SJs (stage 16) (Figure 5-figure supplement 3A). These data suggest that Qsm
395 is not a component of the SG aECM. However, it is possible that the mCh-Qsm signals only detect

396 the cleaved N-terminal fragment of Qsm, while the C-terminal fragment may localize to a different
397 subcellular location. Taken together, our data suggest that Pio and Dpy form filamentous aECM
398 structures in the SG.

399 We next examined Pio, mCh-Pio, Dpy-YFP, and mCh-Qsm signals in *Papss* mutant SGs
400 at stages 14 and 16. At stage 14, Pio antibody and Dpy-YFP signals appeared condensed and
401 enriched within the SG lumen, with reduced association with the apical membrane compared to
402 WT (Figure 5G and G'). Interestingly, Pio antibody signals were barely detectable in the SG
403 lumen at stage 16 (Figure 5H-H'''), likely due to either protein degradation or epitope masking
404 caused by aECM condensation and protein misfolding. In contrast, Dpy-YFP signals remained in
405 the lumen at all stages and were condensed and localized to one side of the lumen at stage 16
406 (Figure 5H-H'''), similar to WGA signals (Figure 2E). mCh-Pio signals were depleted from the
407 expanded region of the lumen but weak signals colocalized with condensed Dpy-YFP signals
408 (Figure 5D). We did not observe any significant differences in the localization or intensity of
409 mCh-Qsm signals in *Papss* mutants (Figure 5-figure supplement 3B and C). These data suggest
410 that the luminal pool of Pio and Dpy, which form filamentous structure, is significantly affected
411 by the loss of *Papss*, resulting in the loss of Pio and the condensation and dissociation of the
412 Dpy-containing aECM structure from the apical membrane.

413

414 **ZP domain matrix is required for uniform SG lumen diameter**

415 We next investigated the role of Pio and Dpy in SG morphogenesis by analyzing SG lumen
416 morphology in *pio* and *dpy* mutants. Immunostaining with Ecad revealed that *pio* null mutants
417 formed relatively normal SGs up to stage 15, but stage 16 SGs showed dramatically abnormal
418 luminal morphology characterized by multiple constrictions, with a slight expansion of the lumen
419 between constrictions (Figure 6A, B and F; Figure 6-figure supplement 1B). The constricted
420 regions were severely narrowed to the point of almost no luminal space, and some luminal regions
421 also showed a flat protrusion on one side of the SG lumen (Figure 6C). Notably, these abnormal
422 luminal shapes were associated with a progressive loss of luminal WGA and Dpy-YFP signals
423 (Figure 6B, D). In *pio* mutants, WGA signals were comparable to WT at stages 13 and 14 (Figure
424 6-figure supplement 1A-B), but appeared slightly reduced and diffuse in the SG lumen at late stage

425 14, and this reduction became more pronounced at stage 15 (Figure 6A and B). Dpy-YFP signals
426 were more severely affected in *pio* mutants. Unlike the strong, filamentous luminal signals in the
427 control (Figure 5-figure supplement 1A), Dpy-YFP signals were reduced and diffuse in the SG
428 lumen and were detected in the cytoplasm of *pio* mutant SG cells from stage 12 to stage 14, with
429 a conspicuous absence in the lumen at stage 15 (Figure 6-figure supplement 1C). By stage 16, both
430 WGA and Dpy-YFP signals were completely absent from the lumen in *pio* mutants, whereas the
431 signals were still present at the apical membrane and in the cytoplasm (Figure 6B and D). We
432 conclude that WGA primarily detects Dpy in the SG lumen and that Pio is required for Dpy
433 secretion to the SG lumen.

434 To test a role for Pio cleavage and localization in shaping the SG lumen, we analyzed embryos
435 mutant for the matriptase Np, which cleaves Pio. In *Np* mutants, Pio and WGA signals were
436 observed in both the apical membrane and lumen up to stage 14, similar to WT embryos (Figure
437 6E). However, at stage 16, Pio signals were observed closely associated with the apical membrane,
438 with no luminal Pio signals present (Figure 6E), suggesting that Np is required for this luminal
439 pool of Pio. Importantly, *Np* mutants exhibited the same bulging and constricting SG luminal
440 phenotype at stage 16 as *pio* mutants (Figure 6E and F), indicating that the filamentous luminal
441 Pio structure plays a crucial role in maintaining a uniform SG diameter.

442 *dpy* mutants (dpy^{ov1}; a spontaneous mutant with a transposable element insertion into intron 11)
443 exhibited a more severe bulging and constriction phenotype in the SG lumen compared to *pio*
444 mutants. Until stage 14, SGs in *dpy* mutants often showed a curved shape, but otherwise had a
445 relatively normal morphology and uniform diameter (Figure 6-figure supplement 1D). At stages
446 15 and 16, SG lumen lost regularity and uniformity, often exhibiting multiple bulges and
447 constrictions. (Figure 6G and G'). In constricting regions, we observed condensed Pio and WGA
448 signals in the lumen, whereas in bulging regions, weak Pio and WGA signals were detected along
449 the apical boundaries (Figure 6G and G'). These data suggest a disrupted luminal scaffold that
450 correlates with the bulging and constricting luminal morphology.

451 To further investigate the role of Np in cleaving Pio to organize the aECM during SG
452 morphogenesis, we overexpressed WT (Np^{WT}) and mutant (Np^{mut}) forms of Np using the UAS-
453 Np-Strep and UAS-Np.S990A-GFP lines (Drees et al., 2019). It should be noted that the
454 endogenous Np remains when either form of Np is overexpressed in the SG. Overexpression of

455 Np^{WT} increased the intensity of luminal mCh-Pio signals (Figure 6H), whereas overexpression of
456 Np^{mut} resulted in the absence of the mCh-Pio signals in the lumen but strong mCh-Pio signals close
457 to the apical membrane and in the cytoplasmic puncta (Figure 6I), supporting the role of Np in
458 cleaving Pio to generate the luminal pool of Pio. In Np^{WT}-overexpressing SGs, the overall intensity
459 of Pio and Dpy-YFP signals also appeared increased at both the apical membrane and in the lumen
460 compared to WT (Figure 6H). These embryos did not show obvious changes in the SG
461 morphology. In Np^{mut}-overexpressing SGs, Pio signals appeared to be increased at the apical
462 membrane, and various levels of filamentous luminal signals were detected (Figure 6I-I'').
463 Importantly, the regions of the lumen lacking luminal Pio signals was always slightly expanded
464 compared to the region with filamentous luminal Pio signals, supporting the idea that the luminal
465 Pio pool is important for a uniform lumen diameter (Figure 6I' and I''; n=11/13). Dpy-YFP signals
466 could not be analyzed properly with Np^{mut} overexpression because of the GFP tag in the Np^{mut}
467 transgene. However, we detected two distinct pools of fluorescent signals in the GFP channel. The
468 first pool was cytoplasmic punctate signals that colocalized with mCh-Pio, which we confirmed
469 are Np^{mut}-GFP signals in a separate staining, and the second pool was thin filamentous luminal
470 signals that overlapped with Pio antibody signals, which we suspect are Dpy-YFP signals (Figure
471 6I). These data suggest that overexpressed Np^{mut} failed to cleave mCh-Pio and Pio, leading to their
472 accumulation at and near the apical membrane, but the endogenous Np still cleaved some pool,
473 resulting in low levels of filamentous luminal Pio structures. Taken together, our data suggest that
474 Dpy and Pio form a luminal scaffold necessary for a uniform SG tube diameter and that Pio
475 cleavage by Np is essential for forming this scaffold.

476

Discussion

Our study highlights the critical role of Papss, a key enzyme that produces the universal sulfate donor PAPS, in aECM organization and lumen expansion in the *Drosophila* embryonic SG. *Papss* mutants show defective SG lumen expansion, accompanied by disruption of the apical domain of SG cells and the aECM. The loss of *Papss* leads to defects in Golgi and intracellular trafficking, abnormal cell death in the SG, and defective basal ECM, emphasizing the importance of sulfation in multiple developmental processes. We also identify the ZP domain proteins Dpy and Pio as key components of the SG aECM, where Dpy is a scaffolding aECM structure that provides mechanical support and Pio is required for proper organization of this structure.

Sulfation is critical for aECM organization and SG lumen expansion

During *Drosophila* SG morphogenesis, secreted cargos are modified in the Golgi, secreted apically, and deposited in the lumen to form the aECM meshwork. Our data show that sulfation is essential for the proper organization of the aECM and the formation of a normal SG luminal shape. Consistent with a high demand for sulfation in the SG, transcripts for *Papss* and several other key enzymes involved in sulfation reactions are also upregulated in the SG, including *slalom* (*sll*), which encodes the *Drosophila* PAPS transporter (Kamiyama et al., 2003; Luders et al., 2003), and *pipe* (*pip*) and *tyrosylprotein sulfotransferase* (*Tpst*), which encode sulfotransferases. Notably, Alcian Blue-stained materials are absent from the SG in *Papss*, *sll*, or *pip* mutants (Zhu et al., 2005), suggesting that sulfation in the SG depends entirely on these enzymes. Our data show that the irregularly expanded SG lumen phenotype in *Papss* mutants is associated with the condensed aECM structures and reduced association of the aECM with the apical membrane (Figures 1 and 2). Inappropriate charge balance due to defective sulfation of proteoglycans and glycoproteins, as well as protein misfolding or failure to bind to appropriate partners, may contribute to aggregation of aECM components and condensation of the aECM structure. The ubiquitously expressed human *Papss1* gene shows upregulation in several glandular organs and the salivary duct (Uhlen et al., 2005; Karlsson et al., 2021), suggesting a potentially conserved role for this enzyme in modifying secreted molecules and modifying aECM in these organs.

506 The defects in SG lumen expansion in *Papss* mutants are linked to defects in intracellular
507 trafficking, characterized by aberrant Golgi structures and mislocalized or reduced levels of
508 several vesicle markers (Figure 3). This suggests that the loss of *Papss* has a broader impact on
509 the intracellular trafficking system, beyond the sulfation of specific substrate molecules. Mutants
510 of the key Golgi component Grasp65 show a mildly irregular SG lumen (Figure 3-figure
511 supplement 3), supporting the important role of the Golgi in establishing proper lumen
512 dimensions during organ formation. Consistent with the idea that the secretory pathway plays a
513 key role in trafficking aECM components to the lumen, several mutants in intracellular
514 trafficking genes, such as *CrebA*, *Sec61β*, and *Sar1*, which encode a major transcription factor
515 that boosts secretory capacity, a Sec61 translocon component, and a COPII vesicle formation
516 component, respectively, have been shown to have a slightly thinner SG lumen (Fox et al., 2013;
517 Fox & Andrew, 2015). However, the defects in *Papss* mutants differ from those in general
518 secretion mutants. While the latter exhibit a uniformly thin lumen, altered localization of several
519 subcellular organelles including mitochondria and the ER, and reduced Golgi signals (Fox &
520 Andrew, 2015), *Papss* mutants show an irregularly expanded lumen and primarily affect the
521 Golgi, while other organelles remain largely intact (Figure 3 and Figure 3-figure supplement 1).
522 Some of the abnormally modified targets appear to be aggregated in the defective Golgi in *Papss*
523 mutants, but many are still transported apically and secreted into the lumen, resulting in a highly
524 condensed luminal aggregate.

525

526 **The role of ZP domain proteins in non-chitinous aECM in the SG**

527 We are beginning to understand the structural components and biological functions of the non-
528 chitinous aECM during tubular organ formation. For example, in the non-chitinous aECM of the
529 *C. elegans* vulva and excretory duct, distinct aECM components, including zona pellucida (ZP)
530 domain proteins, chondroitin proteoglycans, and glycoproteins, work together to form the lumens
531 of these tubular organs (Gill et al., 2016; Cohen, Sparacio, et al., 2020). Our work reveals that
532 two ZP proteins, Dpy and Pio, play essential roles in organizing the aECM in the *Drosophila* SG,
533 highlighting the important role of ZP proteins in forming the non-chitinous luminal matrix
534 during tubular organ formation. Dpy, a gigantic protein (>2 MDa) with hundreds of epidermal
535 growth factor (EGF) repeats interspersed with a Dpy module, forms long filamentous structures

536 (Wilkin et al., 2000). With these filamentous structures, Dpy plays an essential role in the
537 organization and attachment of apical structures in several tissues, including the thoracic cuticle
538 (Wilkin et al., 2000), embryonic trachea (Jazwinska et al., 2003), pupal wings (Bokel et al.,
539 2005), genitalia (Smith et al., 2020), and muscle tendon cells (Chu & Hayashi, 2021). In the SG,
540 aberrantly formed or lost luminal Dpy structures correlate with abnormal luminal morphology
541 (Figures 5, 6 and Figure 5-figure supplement 2). We propose that the Dpy filamentous structure
542 provides mechanical support in the SG aECM and that proper organization of these structures is
543 critical for the formation of a uniform tube diameter. WGA signals always colocalize with Dpy-
544 YFP signals in WT and *Papss* mutants, and both signals are absent from the lumen in *pio*
545 mutants. WGA may primarily detect Dpy in the SG lumen by binding sugar residues that are
546 attached to numerous EGF modules of the Dpy protein. A caveat to the analysis of Dpy using the
547 Dpy-YFP line is that it is a non-functional fusion protein. An antibody against Dpy or a new
548 functional fusion protein will be required to confirm Dpy localization. Even with this caveat, our
549 data with the Pio antibody suggest that Dpy forms the filamentous luminal structure with Pio. Pio
550 is required to secrete and maintain Dpy in the lumen of the SG (Figure 6). This is consistent with
551 a role for Pio in Dpy secretion in the *Drosophila* trachea (Drees et al., 2023) and suggests a
552 conserved role for Pio in multiple tissues. Since the ZP domains of Pio and Dpy have been
553 shown to bind directly to each other in vitro (Drees et al., 2023), it is likely that the binding of
554 Pio and Dpy is required for the formation of filamentous luminal structures. This binding may
555 require cleavage of Pio by the matriptase Np, which generates the filamentous luminal pool of
556 Pio (C-terminal ZP fragment of Pio). *pio* and *Np* mutants show similar bulging and constricting
557 SG lumen morphology (Figure 6), suggesting that the generation of the C-terminal ZP fragment
558 of Pio by Np is critical for the formation of the filamentous luminal structure with Dpy.

559 Papss plays an essential role in the formation of the filamentous Dpy/Pio structure
560 (Figure 5). It will be important to learn if the defects of the Pio-Dpy matrix in *Papss* mutants is a
561 direct consequence of the loss of sulfation on these proteins or if it's an indirect outcome. The ZP
562 domain can mediate homomeric or heteromeric polymerization into filaments, and its structure is
563 stabilized by disulfide bonds formed between conserved Cys residues responsible for the
564 polymerization of ZP modules (Jovine et al., 2002). Defective disulfide bond formation due to
565 defective sulfation may destabilize Pio-Dpy interactions. Additionally, hundreds of EGF
566 modules in the Dpy protein are highly susceptible to O-glycosylation. Sulfation of the glycan

567 groups attached to Dpy may be critical for its ability to form a filamentous structure. In the
568 absence of sulfation, the glycan groups on Dpy may not properly interact with the surrounding
569 materials in the lumen, resulting in an aggregated and condensed structure.

570 It will be interesting to determine the role of other ZP proteins highly expressed in the SG.
571 Qsm, for example, has been found in the same intracellular vesicles as Dpy in *Drosophila* tendon
572 cells and has been shown to physically interact with Dpy through their ZP domains (Chu &
573 Hayashi, 2021). Qsm has been shown to remodel Dpy filaments that link tendon cells to the pupal
574 cuticle, increasing their tensile strength (Chu & Hayashi, 2021). In the SG, we find that Qsm is
575 mainly localized to cytoplasmic vesicles and AJ/SJ regions rather than being present in the SG
576 lumen like Pio and Dpy. It should be noted that like Pio, Qsm has a furin cleavage site near the
577 transmembrane domain and another putative protease cleavage site in the ZP domain. Since the
578 mCh-Qsm line contains the mCh insertion near the N-terminal end of the protein, the mCh-Qsm
579 signals are likely those of the cleaved N-terminal fragment after cleavage by these proteases and
580 will need to be confirmed using western blot. Further investigation will be needed to determine
581 the role of Qsm in junctional regions of SG cells. Also, the roles of other SG-upregulated ZP
582 domain proteins remain to be elucidated.

583 In conclusion, our analysis of the *Drosophila Papss* gene, a single ortholog of human
584 Papss1 and Papss2, reveals its multiple roles during SG development. We expect that these
585 findings will provide important insights into the function of these enzymes in normal
586 development and disease in humans. Our findings on the key role of two ZP proteins, Pio and
587 Dpy, as major components of the SG aECM also provide valuable information on the
588 organization of the non-chitinous aECM during organ formation.

589

590 **Materials and Methods**

591 **Fly stocks and genetics**

592 The fly stocks used in this study are listed in Table S2. All the crosses were performed at 25°C.

593

594 **Generation of transgenic lines**

595 UAS lines for the Papss-PD (657 aa) and Papss-PE/F/H (630 aa; hereafter referred to as Papss-
596 PE) isoforms were generated. Papss-PD and Papss-PE differ only slightly in the N-terminus.
597 Two UAS clones, UFO09742 (DGRC Stock 1643418;
598 https://dgrc.bio.indiana.edu//stock/1643418 ; RRID:DGRC_1643418) and UFO09743 (DGRC
599 Stock 1643419 ; https://dgrc.bio.indiana.edu//stock/1643419 ; RRID:DGRC_1643419), were
600 obtained from the *Drosophila* Genomics Resource Center. UFO09742 was generated from the
601 RE15281 cDNA clone encoding the open reading frame (ORF) for the Papss-PD isoform.
602 UFO09743 was generated using the RE03925 cDNA clone, which encodes the same ORF for the
603 Papss-PE isoform. Each clone contains a C-terminal Flag-HA tag. Purified DNA for the UAS
604 clones (500 ng/µl) was sent to GenetiVision (Houston, TX) for injection. GenetiVision
605 performed PhiC31-mediated insertions using the attP40 site.

606 UAS-Papss mutant lines for the APS kinase and ATP sulfurylase domains were generated
607 by site-directed mutagenesis using the UAS-Papss-PD construct (UAS-Papss-PD^{K193A}, UAS-
608 Papss-PD^{F593P}, and UAS-Papss-PD$^{K193A, F593P}$). K161 and F550 in human Papss (K193 and F593
609 residues of *Drosophila* Papss-PD*)* were identified as being critical for the catalytic efficiency of
610 the APS kinase and ATP sulfurylase domains, respectively (Zhang et al., 2022; Zhang et al.,
611 2023), and were mutated to alanine and proline, respectively. The UAS-Papss-PD construct was
612 amplified using the NEB Q5 master mix and the following primers.

613 **Primers used to make *UAS-Papss-PD^{K193A}***

614 Primer forward: 5'-CCGGGACGTGGCGGGTCTATACAAG-3'

615 Primer reverse: 5'-GTTTCGCACACATCCAG-3'

616 **Primers used to make *UAS-Papss-PD^{F593P}***

617 Primer forward: 5'-GATCCTGCCCCCGCGTGTTGCTG-3'

618 Primer reverse: 5'-TCCATGCTGTCTAGTC-3'

619 Following amplification, a kinase, ligase, and DpnI (KLD) reaction was performed and the
620 mutant construct was transformed into DH5α competent cells. To screen for colonies containing
621 a correct mutation, plasmid DNAs were isolated and the ORF of *Papss* was sequenced using the
622 following primers.

623 **Primers for sequencing the *Papss* ORF**

624 **Forward primer 1:** 5'-TGACCGAGCAAAAGCACCAT-3'

625 **Forward primer 2:** 5'-CGAGGTGGCCAAGTTGTTTG-3'

626 **Forward primer 3:** 5'-CCCGAGTTCTACTTTCAGCGT-3'

627 **Forward primer 4:** 5'-GCCGGTGCGAACTTCTACAT-3'

628 **Reverse primer:** 5'-ATACCAGGTACGCCTCCAGT-3'

629 To ensure no secondary mutations are present, the Papss ORF containing the correct mutations
630 was ligated with the original backbone of the UAS-Papss construct. The construct containing
631 both the K193A and F593P mutations was generated by combining DNA fragments containing
632 each mutation, which were obtained by digesting the respective K193A and F593P constructs,
633 and ligating them to a UAS backbone. Midi-prepped DNA samples were sent to GenetiVision
634 (Houston, TX) for a PhiC31 injection.

635

636 **Immunostaining and confocal microscopy**

637 *Drosophila* embryos were collected on a grape juice agar plate. All embryos were dechorionated
638 by incubation in 50% bleach for three minutes at room temperature. After dechorionation,
639 embryos were fixed in either saturated heptane or standard formaldehyde fixative (7 ml heptane,
640 5.6 ml ddH_2O, 700 µl 37% formaldehyde, 700 µl 10x PBS). Saturated heptane was prepared by

641 mixing heptane:37% formaldehyde 1:1 and shaking vigorously. For immunofluorescence
642 staining, embryos were fixed in saturated heptane for forty minutes at room temperature,
643 devitellinized by vortexing in 80% ethanol, and then washed three times in absolute ethanol. For
644 staining using the horseradish peroxidase (HRP) reaction for visualization, embryos were fixed
645 in formaldehyde fixative and devitellinized by vortexing in 100% methanol. Embryos were then
646 stained with primary and secondary antibodies in PBSTB (1X PBS, 0.2% bovine serum albumin,
647 and 0.1% Triton X-100). All antibodies used are listed in Table S3. Embryos were then mounted
648 in Aqua-Poly/Mount (Polysciences, Inc). Confocal images were taken using a Leica TCS SP8
649 confocal microscope with 63x, NA 1.4 and 40x, NA 1.3 objectives. HRP images were taken
650 using a Leica DM2500 microscope using a 20x, 0.8 NA objective.

651

652 **Fluorescence in-situ hybridization**

653 In situ hybridization in WT embryos was performed as described in Knirr et al., 1999. Embryos were
654 fixed in a standard formaldehyde fixation, followed by devitellinzation by 100% methanol. To make the
655 *Papss* mRNA probe that detects all splice forms, a 799 bp portion of the *Papss* ORF was amplified
656 using the *UAS-Papss-PD* construct as a template. To make isoform-specific mRNA probes, unique
657 sequence segments common to specific *Papss* isoforms were identified using Flybase sequences and
658 used to design primers for PCR amplification, using WT genomic DNA as a template. The primers are
659 listed below.

660

Papss isoform	Primer sequence	Product size
All isoforms	Forward Primer: 5'-ACAAGGATGCGGGTCTGAAG-3' Reverse Primer: 5'-G<u>ATTTGGTGACACTATAG</u>CGCCTTAACTCGTTGGGAG-3'	799 bp
ABCFG	Forward primer: 5'-	106 bp

	TTCGCAGTTTTGTTTGGAAT-3’ Reverse primer: 5'- GATTTAGGTGACACTATAGTGCTCTCCGG AACTTCACTCAT-3'	
EFH	Forward primer: 5'- TTCGCTTTCGACGTTCGTCG-3' Reverse primer: 5'- GATTTAGGTGACACTATAGCTTCTTTTGA TATGGGGATAAAA-3'	228 bp
DH	Forward primer: 5'- TTCACCTGCCCAACGTTTCG-3' Reverse primer: 5'- GATTTAGGTGACACTATAGCAAGCGCTGT TGTTATTGTTAA-3'	106 bp

661 *SP6 RNA polymerase promoter sequence underlined

662

663 Digoxigenin (DIG)-labeled RNA probe was generated by transcribing amplified and purified
664 DNA using SP6 RNA polymerase and DIG RNA labeling mix (Sigma). Following hybridization,
665 the RNA probe was detected using a sheep α-DIG antibody (Enzo; ENZ-ABS302-0001;
666 1:1,000). The secondary antibody, α-sheep IgG conjugated with biotin (Invitrogen; 1:500), was
667 visualized using a tyramide reaction with Cy3 (Perkin Elmer Life Sciences, NEL753001kt;
668 1:50). The embryos were mounted in Aqua-Poly/Mount. Confocal images were taken using a
669 Leica TCS SP8 confocal microscope with 63x, NA 1.4 and 40x, NA 1.3 objectives.

670

671 **Genomic DNA sequencing of the Papss open reading frame region in *Papss*^{2} mutant**

672 *Papss*^{2} homozygous mutant embryos were sorted for GFP signals in the balancer chromosome, and
673 genomic DNA was extracted from them. The open reading frame of *Papss* was amplified using the
674 isolated genomic DNA as a template, with the following primers.

675 Primer forward *Papss*: 5'-CTACAGGTGGCGACGAATGT-3'

676 Primer reverse *Papss*: 5'-GCGGCAGGTTCTGGTAGTAG-3'

677 Sanger sequencing of the amplified DNA segment of *Papss* was performed using the primers
678 below.

679 Forward primer 1: 5'-ACAGGTGGCGACGAATGTG-3'
680 Forward primer 2: 5'-TGACCGAGCAAAAGCACCAT-3'
681 Forward primer 3: 5'-CGAGGTGGCCAAGTTGTTTG-3'
682 Forward primer 4: 5'-CCCGAGTTCTACTTTCAGCGT-3'
683 Forward primer 5: 5'-GCCGGTGCGAACTTCTACAT-3'
684 Reverse primer: 5'-GCGGCAGGTTCTGGTAGTAG-3'
685

686 **Quantification of SG cell number**

687 Confocal images immunolabeled with CrebA for stage 16 SGs were used. 3D images for SGs were
688 generated using Imaris (Andor), and SG nuclei were counted using cell ID numbers. Data were
689 displayed using GraphPad Prism, and statistical significance was determined by one-way ANOVA.

690

691 **Quantification of SG lumen area**

692 Confocal images immunolabeled with Ecad for stage 16 SGs were used. Z-stacks were merged to
693 encompass the entirety of the SG lumen. Using Fiji (NIH), images were set to scale according to image
694 properties listed in LasX files. The polygon selection tool was used to outline the entirety of the SG
695 lumen, excluding the SG duct. SG lumen areas were determined for WT, *Papss* thin, and *Papss*
696 irregularly expanded respectively. Statistical significance was determined using a nonparametric t-test as
697 the data did not fit a Gaussian distribution. Sample numbers are: n=16, WT; n=13, $Papss^2$ with a thin
698 lumen; n=11, $Papss^2$ with an irregularly expanded lumen; n=8, $Papss^2/Df$ with a thin lumen; n=8,
699 $Papss^2/Df$ with a irregularly expanded lumen; n=10, *sage>Papss* with a normally expanded lumen; n=8,
700 *sage>Papss-PE;* $Papss^2$ with a normally expanded lumen; n=10, *sage>Papss-PD;* $Papss^2$ with a

701 normally expanded lumen; n=11, *sage>Papss-PD*^{K193A,F593P}*; Papss*^{2} with a thin lumen; n=7,
702 *sage>Papss-PD*^{K193A,F593P}*; Papss*^{2} with a irregularly expanded lumen.

703

704 **Quantification of SG lumen length and diameter**

705 Confocal images of stage 16 SGs immunolabeled with an antibody for the cell junction marker, E-cad,
706 were used. Several Z-sections, spanning approximately half of the circumferential/radial axis of the SG
707 lumen, were merged to create a projection which covered the entire length of the lumen. The line tool in
708 Fiji was used to measure the length of the SG lumen. To measure the diameter of the SG lumen, the
709 lumen was divided into four equal segments using the lumen length obtained above, as there are
710 sometimes minor variations in width value along the length of the lumen. The line tool in Fiji was then
711 used to measure the width along each quarter of the lumen, and an average value was obtained per SG.
712 Each measurement obtained in Fiji was adjusted for scale according to the image properties in the raw
713 confocal file. Sample numbers are: n=8, WT; n=8, *Papss*^{2} with a thin lumen; n=10, *Papss*^{2} with an
714 irregularly expanded lumen; n=8, *Papss*^{2}*/Df* with a thin lumen; n=8, *Papss*^{2}*/Df* with a irregularly
715 expanded lumen; n=10, *sage>Papss-PE* with a normally expanded lumen; n=8, *sage>Papss-PE; Papss*^{2}
716 with a normally expanded lumen; n=10 *sage>Papss-PD; Papss*^{2} with a normally expanded lumen;
717 n=11, *sage>Papss-PD*^{K193A,F593P}*; Papss*^{2} with a thin lumen; n=7, *sage>Papss-PD*^{K193A,F593P}*; Papss*^{2} with
718 a irregularly expanded lumen.

719

720 **Quantification of Crb signal intensity**

721 Confocal images of stage 16 SGs immunolabeled with antibodies against the sub-apical region (SAR)
722 marker, Crb, and the AJ marker, Ecad, were used. A maximum intensity projection of the apical region
723 of several SG cells with the highest Ecad and Crb signals was created using seven z-sections. Regions
724 were manually drawn along the inner or outer boundary of the Ecad signals of each cell to mark the
725 SAR and apical-medial regions. The mean gray value of the apical-medial Crb signals in each cell (the
726 region delineated by the inner boundary of the Ecad signals) was quantified using Fiji. The mean gray
727 value of the SAR Crb signals was calculated using the integrated densities and areas calculated with Fiji
728 for regions between inner and outer boundaries. To subtract the background, the average mean gray

729 value of Crb signals for five regions outside the embryo was subtracted from the mean gray values of the
730 SAR and apical-medial Crb signals in each SG cell. The ratio of the SAR to the apical-medial Crb level
731 was compared. Seven and six embryos were used for the WT and *Papss* mutants, respectively, and four
732 to eight cells per SG. SuperPlots were used to address variability in the data sets of each SG. Statistical
733 significance was determined using a Welch's t-test.

734

735 **Quantification of the number and signal intensity of WGA puncta**

736 High-resolution confocal images of stage 16 SGs immunostained with CrebA (SG nuclei), Ecad, and
737 WGA were obtained using an Olympus SpinSR10 Sora spinning disk confocal microscope with a 100x,
738 NA 1.5 objective. Each image was taken under identical imaging conditions. Three-dimensional (3D)
739 reconstruction of the WGA puncta was obtained using the Imaris software (Andor), and the number of
740 puncta per SG was counted by Imaris. The Imaris machine learning tool was used to exclude non-puncta
741 WGA signals within the SG and non-SG WGA puncta. After 3D reconstruction, the pixel intensity of
742 each WGA punctum was also obtained and used for further analysis.

743

744 **Quantification of WGA and ManII-GFP signal intensity**

745 Confocal images of stage 16 SGs immunostained for WGA and ManII-GFP were used. Single z-sections
746 of each image were imported into Fiji, and a line intensity profile was generated using the Line Tool and
747 Color Profiler pluggin. Lines were drawn across regions spanning two ManII-GFP/WGA puncta, and
748 the signal intensities for each pixel along the line for both ManII-GFP and WGA channels were
749 obtained.

750

751 **Quantification for Rab11 and Sec15 apical region intensity**

752 Single z-sections halfway through the proximal-distal axis from confocal images for stage 16 SGs
753 immunolabeled for Rab11 or Sec15 and Ecad were used for quantification. Threshold images for Sec15
754 or Rab11, which display pixels as black or white based on whether they are above a value for signal
755 intensity, were generated in Adobe Photoshop. In addition, Sec15 and Rab11 images were converted

using the RGB stack function in Fiji. A stack of images including the threshold and RGB stack converted images for Sec15 or Rab11 and the Ecad images was generated using the images to stack function in Fiji. Using the threshold images for Sec15 and Rab11, a boundary for the apical region encompassing five SG cells, and the mean gray value intensity was calculated from the RGB stack converted Rab11or Sec15 images. The graph was generated in GraphPad Prism, and statistical significance was calculated using Welch's t-test.

Quantification for Rab7 puncta number and intensity

Single z-sections halfway through the proximal-distal axis from confocal images for stage 16 SGs immunolabeled for Rab7 and Ecad were used for quantification. Threshold images for Rab7, which display pixels as black or white based on whether they are above a value for signal intensity, were generated in photoshop. Rab7 images were converted using the RGB stack function in Fiji. A stack of images including the threshold and RGB stack converted images for Rab7 and Ecad images were generated using the images to stack function in Fiji. Using the threshold images for Rab7, a boundary was drawn around all puncta present in five cells for each sample, and the mean gray value intensity and area was calculated for the RGB stack Rab7 converted image. The average mean gray value of punctate intensity and the average number of punta in each cell were calculated using Fiji. Punta with an area greater than or equal to 0.100 μm^2 were used for quantification. Statistical significance was calculated by Welch's t-test using GraphPad Prism.

Quantification of the number of dying cells

Confocal images of stage 16 SGs that were immunolabeled with antibodies against CrebA (to mark the SG nucleus), and DCP-1 (a cell death marker) were used. The number of regions within the SG with DCP-1 signals and/or blank spots where CrebA signals should have been present were counted manually.

Transmission electron microscopy (TEM)

783 Stage 15 embryos were fixed in 2% glutaraldehyde in 0.2 M phosphate buffer pH 7.4 and rinsed
784 4 times in 0.1 M phosphate buffer pH 7.2 containing 0.02 M glycine. Embryos were post-fixed in
785 2% osmium tetroxide for 1 hour in the dark, rinsed 3 times in dH_2O, stained en bloc in 1% uranyl
786 acetate for 1 hour in the dark, and rinsed 3 times in dH_2O. Samples were dehydrated in a series
787 of ethanol and then propylene oxide twice. Embryos were then infiltrated in propylene oxide:
788 Epon resin series and embedded in Epon at 60ºC for 24 hours. Semi-thin sections were
789 performed followed by Toluidine Blue staining to obtain a salivary gland section. Ultra-thin
790 sections for TEM were cut on a Leica EM UC7 microtome. TEM sections were mounted on
791 carbon-coated copper grids (EMS FCF-150-CU), stained with 2% uranyl acetate and Reynolds
792 lead citrate, and the ultra-thin sections were viewed on a JEOL JEM-1400, 120kV transmission
793 electron microscope and imaged with a Gatan digital camera. Sections from at least five
794 independent embryos were analyzed for wild type and *Papss* mutants.

795

796 **Figure legends**

797 **Figure 1. *Papss* mutants show defects in SG lumen expansion.** (A) Stage 16 SGs
798 immunostained for Stranded at Second (SAS). (B) In situ hybridization using an antisense probe
799 for *Papss* mRNA in WT embryos. (C-H) Stage 14 and stage 16 SGs immunostained for Ecad
800 and CrebA. Yellow asterisks indicate regions of irregular, non-uniform expansion (D, E, H) or
801 over-expansion (G) of the SG lumen. (I, I') Quantification of different SG lumen phenotypes. (J)
802 Quantification of SG lumen length. n=7-11 SGs for each genotype. See the Materials and
803 Methods for the sample size of each genotype. One-way ANOVA test with multiple comparison
804 (*, $p<0.05$; ns, non-significant). (K, K') Quantification of the SG lumen diameter (K) and the
805 coefficient of variation for each SG (K'). The diameter is measured in three different regions of
806 the lumen. The average diameter, as well as the individual data points, are shown. The same
807 samples are used for the quantifications in J-K'. One-way ANOVA test with multiple
808 comparison (***, $p<0.001$; ns, non-significant) (L) Quantification of SG lumen area. n=7-16
809 SGs for each genotype. One-way ANOVA test with multiple comparison (***, $p<0.001$; ****,
810 $p<0.0001$; ns, non-significant). Horizontal lines indicate mean values.

811 **Figure 2. Mutations in *Papss* result in mislocalized Crb and disruption of the aECM**
812 **architecture.** (A) Cartoon showing the subcellular localization of Crb in SG cells. (B, C) Stage
813 16 SGs immunostained for Crb and Ecad. Magnified images are shown for yellow dotted boxed
814 regions. (D) Quantification of the Crb signal intensity ratio between the SAR and apical-medial
815 regions of SG cells. (n=7, WT; n=6, $Papss^2$ (4-8 cells per SG)). Student's T-test with Welch's
816 correction (***, $p<0.001$). (E-G) Stage 16 SGs stained for Ecad and wheat germ agglutinin
817 (WGA). Magnified images are shown for the boxed regions. Arrows, WGA localization at the
818 apical membrane in WT (yellow) and *Papss* mutant (cyan) SGs. Yellow arrowhead in E, WGA
819 localizes as thin filaments in the lumen of WT SG. Cyan arrowheads, WGA localizes as a highly
820 condensed structure in the thin luminal region of the *Papss* SG. White arrowheads, WGA
821 localizes as a condensed, filamentous structure in the expanded luminal region of the *Papss* SG.
822 Yellow arrowheads in G, WGA localizes as a mildly condensed filament in the lumen of
823 *sage>Papss-PE; $Papss^2$* SG. (H, I) TEM images of stage 15 SGs. SGs are pseudo-colored in
824 magenta. Magnified images of the luminal areas (boxed regions) are shown in the bottom.
825 Yellow asterisk in H, electron-dense luminal material in WT SG. Cyan asterisks in I, condensed

826 electron-dense luminal material in the *Papss* mutant SG. Green asterisk, a large luminal area
827 lacking electron-dense material in the *Papss* mutant SG.

828 **Figure 3. Loss of *Papss* results in disorganized Golgi structures and defects in intracellular**
829 **trafficking components.** (A-D) Stage 16 SGs stained with WGA. Magnified images are shown
830 for the boxed regions. Yellow arrows, WGA signals as cytoplasmic puncta. Cyan arrows, WGA
831 signals in the nuclear envelope. (E-H) Three-dimensional (3D) reconstruction of cytoplasmic
832 WGA puncta in stage 16 SGs. (I, I') Quantification of the number of WGA puncta (I) and signal
833 intensity (I') within SG cells. n=5 SGs for all genotypes, except WT in G (n=6). One-way
834 ANOVA test with multiple comparisons (**, $p<0.01$; ***, $p<0.001$; ns, non-significant).
835 Horizontal lines indicate mean values. (J, K) Stage 16 SGs stained for GFP (for ManII-GFP) and
836 WGA. Magnified images are shown for the boxed regions. Yellow arrows in J, ManII-GFP and
837 WGA puncta colocalize in WT SG. Asterisks in K, dispersed ManII-GFP signals in *Papss*
838 mutants. Cyan arrows in K, little colocalization of ManII-GFP and WGA in the *Papss* SG. (L,
839 L') Line intensity profile showing the signal intensity of ManII-GFP (green) and WGA
840 (magenta) along the yellow and cyan dotted lines in J and K, respectively. (M, N) TEM images
841 of the Golgi. Yellow arrows in M, Golgi structures in WT SG cells. Magenta arrows in N, Golgi
842 structures in the *Papss* SG. Cyan arrows in N, electron-dense structures in the Golgi of *Papss*
843 mutant SG cells. (O, P) Stage 16 SGs immunostained for Rab11 and Ecad. Magnified images are
844 shown for boxed regions. Rab11 signals at the apical membrane are increased in *Papss* mutants
845 (cyan arrowheads in P) compared to WT (yellow arrowheads in O), with occasional large
846 punctate signals mislocalized to the basolateral domain (cyan arrow in P). (Q, R) Stage 16 SGs
847 immunostained for Sec15 and Ecad. Compared to strong apical Sec15 signals in the WT SG
848 (yellow arrowheads in Q), Sec15 signals are reduced in *Papss* mutants (cyan arrowheads in R).
849 (S, T) Quantification of the intensity of Rab11 (S) and Sec15 (T) at the apical membrane regions
850 in WT and *Papss* mutant SGs. Welch's t-test (**, $p<0.05$). Horizontal lines indicate mean values.
851 (U, V) TEM images for the apical region of SG cells. Yellow arrowheads, electron-dense
852 vesicles in both genotypes. Red arrowheads, empty, larger vesicle-like structures in *Papss*
853 mutants. (W) Quantification of the electron-dense vesicle numbers per cell slice. Welch's t-test
854 (**, $p<0.05$). Horizontal lines indicate mean values.

855

856 **Figure 4. *Papss* mutants show premature SG cell death.** (A, B) Stage 16 SGs immunostained
857 for CrebA, DCP-1 and Ecad. Cross-sectional images are shown for the yellow dashed line in B.
858 Yellow arrowheads, DCP-1 signal is detected in the SG in *Papss* mutants. White dashed lines,
859 the basal boundary of the SG. (C) TEM image of stage 15 SG cells, including a dying cell
860 (yellow arrow). Cyan arrows, nuclei of normal living cells. (D) Quantification of the number of
861 acellular regions in stage 16 SGs. (n=8 SGs, WT; n=10, $Papss^2$; n=15, *sage>Papss-PD;* $Papss^2$;
862 n=8, *sage>Papss-PD*^{K193A,F593P}; $Papss^2$) (E) Quantification of the number of SG cells at stage 16
863 (n=10 SGs, WT; n=10, $Papss^2$; n=8, $Papss^2$/*Df*; n=8, *sage>p35;* $Papss^2$; n=10, *sage>Papss-PE;*
864 $Papss^2$; n=8, *sage>Papss-PD*^{K193A,F593P}; $Papss^2$). One way ANOVA test (****, $p<0.0001$; ns,
865 non-significant). (F, G) Stage 16 SGs immunostained for CrebA, Ecad, and mCherry (for
866 Hemo3x-mCh). Cross-section images are shown for the yellow dashed lines. White dashed lines,
867 the basal boundary of the SG. Yellow arrowhead in F, hemocyte signals outside of the control
868 SG. White arrowhead in G, hemocyte signals are present inside the SG in *Papss* mutants. (H, I)
869 Stage 16 SGs immunostained for DAPI, mCh (for Hemo3x-mCh), and Ndg. Magnified views are
870 shown for boxed regions. Yellow dashed lines, the basal boundary of the SG. (H) In WT,
871 hemocytes are found outside of the SG (yellow arrowheads), with Ndg forming a barrier at the
872 basal boundary of the SG (yellow arrows). (I) In *Papss* mutants, hemocytes invade the SG
873 epithelia (white arrowheads), where Ndg signals are irregular or absent (white arrows).

874 **Figure 5. Loss of *Papss* disrupts the localization of Dpy and Pio in the aECM.** (A) Stage 16
875 SGs stained for a chitin-binding protein (CBP) and Ecad. (B) Cartoon of the mCh-Pio fusion
876 protein showing the region for the antibody and protease cleavage sites. (C, D) Stage 14 and
877 stage 16 SGs immunostained for mCh (for mCh-Pio) and GFP (for Dpy-YFP). The mCh-Pio
878 (white arrowheads) and Dpy-YFP (cyan arrowheads) signals are largely absent from the
879 expanded region of the lumen. Along one side of the lumen, weak mCh-Pio signals colocalize
880 with condensed Dpy-YFP signals (yellow arrows). (E-H’’’) Stage 14 and stage 16 SGs
881 immunostained for Pio, GFP, and Ecad. Magnified images of boxed regions in E-H and shown in
882 E’-H’’. F’’ and H’’’ are cross-sectional images of the SG lumen for regions indicated by white
883 lines F’ and H’’. Yellow arrowheads, Pio and Dpy localized to the apical membrane. Cyan
884 arrowheads, Dpy and Pio localized to the SG lumen. Note a higher proportion of Dpy and Pio
885 localized to the lumen in the *Papss* mutant SG at stage 14 (cyan arrowheads in G’). White

886 arrowheads in H'-H''', Dpy accumulates towards one side of the lumen in the stage 16 *Papss*
887 SG. Yellow asterisks, Pio is absent from the lumen at stage 16 in the *Papss* SG.

888 **Figure 6. Pio is essential for uniform SG lumen diameter by maintaining Dpy in the lumen.**
889 (A, B) SGs at stages 13-16 stained for WGA and Ecad. Yellow arrowheads in A, filamentous
890 luminal WGA signals. Cyan arrowheads in B, WGA signals at the apical membrane. Yellow
891 asterisks, loss of lumina WGA signals. White arrowheads, constricted lumen. (C) Stage 16 SGs
892 immunostained for Ecad and CrebA. Cross sectional images for the yellow and green dotted
893 lines are shown on the right. Yellow arrowhead, flat protrusion of the lumen. Green arrowhead,
894 constricted lumen. (D) Stage 16 SGs stained for Ecad and GFP (for Dpy-YFP). Projection
895 images contain merged z-sections, from the apical surface of the SG cells to midway through the
896 SG. Single section, one z-section at the approximate midpoint of the lumen width. Yellow
897 arrowhead, area of constricted lumen. Yellow asterisk, luminal area with no Dpy-YFP signals.
898 (E) Single z-sections of confocal images of SGs at stages 15 and 16 stained for Ecad, Pio and
899 WGA. White arrowheads, area of constricted lumen. Yellow asterisks, no luminal signals of
900 WGA and Pio. (F) Quantification of the number of constrictions in the SG lumen at stage 16
901 (n=7 for both genotypes). (G, G') SGs at stages 14-16 stained for Ecad, WGA and Pio. Higher
902 magnification of the yellow boxed regions is shown in G'. (H, I) Stage 16 SGs overexpressing
903 Np^{WT} (H) or Np^{mut} (I) that are immunostained for GFP (for Dpy-YFP and Np-GFP), Pio, and
904 mCh (for mCh-Pio). Np^{WT}-overexpressing SGs show strong, uniform mCh-Pio signals in the
905 lumen (cyan asterisks in H), whereas Np^{mut}-overexpressing SGs shows no detectable signals in
906 the lumen (cyan asterisk in I). In Np^{WT}-overexpressing SGs, the luminal mCh-Pio signals are so
907 bright that the cytoplasmic, punctate mCh-Pio signals are rarely detectable alongside the luminal
908 signals. Increasing the brightness to visualize the cytoplasmic punctate signals shows very strong
909 luminal mCh-Pio signals (inset in H). Np^{WT} overexpression shows high levels of Pio (magenta
910 arrowheads in H) and dpy-YFP (green arrowheads in H) signals in both the apical membrane and
911 lumen. In contrast, Np^{mut} overexpression shows strong Pio signals in the apical membrane and
912 various levels of Pio in the lumen. (I', I'') Higher magnification of the yellow boxed regions.
913 The lumen diameter of the region with undetectable luminal Pio levels is slightly larger (magenta
914 asterisk) compared to the region with clear luminal Pio signals (magenta arrowheads).

915

916 **Figure 7. A proposed model.** (A) Cartoon diagram showing normal lumen expansion in WT SG
917 and defective luminal morphology in *Papss*, *pio*, and *Np* mutants. (B) Organization of the ZP
918 domain protein-containing aECM in the SG. In WT, the ZP-C fragment of Pio (which is cleaved
919 by Np and furin proteases) forms a complex with Dpy to build a filamentous scaffold within the
920 lumen. In *Papss* mutants, this fragment is absent from the lumen at stage 16, and the Dpy-
921 containing aECM structure becomes aggregated and highly condensed. The absence of luminal
922 Pio in *pio* and *Np* mutants results in the loss of luminal Dpy and lumen constrictions.

923

Acknowledgements

We thank the members of the Chung laboratory for their comments and suggestions. We thank M. Behr, S. Hayashi, the Bloomington stock center (NIH P40OD018537), and the Kyoto *Drosophila* stock center at Kyoto Institute of Technology for fly stocks. We thank M. Affolter for the Pio antibody. Many antibodies were obtained from the Developmental Studies Hybridoma Bank, created by the NICHD of the NIH and maintained at The University of Iowa, Department of Biology, Iowa City, IA 52242. cDNAs for *Papss* were obtained from the *Drosophila* Genomics Resource Center (NIH 2P40OD010949). Confocal and electron microscopy were performed at the Shared Instrumentation Facility (SIF) at Louisiana State University. The model in Figure 7 was created in https://BioRender.com. This work was supported by the National Science Foundation (MCB 2141387) and National Institutes of Health (R03DE034704) to SC.

937 **Table S1. A targeted Df screen revealed Papss as a key enzyme for SG lumen expansion.**

SG-upregulated enzymes	Predicted roles	Df lines tested	SG lumen shape
CG17633	Metallocarboxypeptidase	Exel6024	Disrupted embryo morphology
CG30283	Serine-type endopeptidase	Exel6076	Disrupted embryo morphology
Papss	PAPS synthetase	Bsc445	Thin SG lumen with apical protrusions
PH4αSG1/SG2	Prolyl 4-hydroxylase	Exel6216	Non-uniform lumen diameter
CG16758	Purine nucleotide phosphorylase	Bsc116	Non-uniform lumen diameter
CG8708	N-acetylgalactosaminide β-1,3-galactosyltransferase	Exel7095	Irregular apical membrane
CG7920	Acetate CoA-transferase	Bsc620	Irregular apical membrane
Pgant6	Polypeptide N-acetylgalactosaminyltransferase	Exel6091	Irregular apical membrane
GlcAT-P	Glucuronosyltransferase	Bsc817	Irregular apical membrane
CG34290	Serine-type endopeptidase	Bsc638	Irregular apical membrane
Peroxidasin	Bromide peroxidase	Bsc119	Irregular apical membrane
ScsβG	Succinyl Co-A synthetase β subunit	Bsc387	Short and rounded SG

938

939 **Table S2. Fly strains used**

Fly strain	**Sources and References**	**RRID**
Oregon R (wild type)		
sage-Gal4	Chung et al., 2009	
fkh-Gal4	Henderson and Andrew, 2000	
Papss^{2}	Bloomington Stock Center	BDSC_26171
UAS-p35	Bloomington Stock Center	BDSC_5072
UAS-Papss-PD	This work	
UAS-Papss-PE	This work	
UAS-Papss-PD$^{K193A,\ F593F}$	This work	
Dpy-YFP	Kyoto stock center	DGGR_115238
SrpHemo3x-mCherry	Gyoergy et al., 2018	BDSC_78358
Dp-YFP, mCh-Qsm	Chu and Hayashi, 2021	
mCh-Qsm	Chu and Hayashi, 2021	
Dpy-YFP, mCh-Pio	Drees et al., 2023	
UAS-ManII-GFP	Bloomington stock center	BDSC_65248
UAS-GFP-KDEL	Bloomington stock center	BDSC_9898
pio^{17c}	Drees et al., 2023	
Np^{C2}	Drees et al., 2023	
dpy^{ov1}	Bloomington stock center	BDSC_276
Grasp65^{102}	Zhou et al., 2014	BDSC_65257
GM130$^{\Delta 23}$	Zhou et al., 2014	BDSC_65255

UAS-Np.WT-Strep	Drees et al., 2019	
UAS-Np.S990A-GFP	Drees et al., 2019	

940

941

942 **Table S3. Antibodies Used**

Antibody	Source	RRID	Dilution
α-Ecad (rat)	DSHB (DCAD2)	AB_528120	1:50
α-CrebA (rat)	Andrew lab (John Hopkins University); re-made in this study		1:3,000
α-CrebA (rabbit)	Andrew lab (John Hopkins University)	AB_10805295	1:5,000
α-CrebA (guinea pig)	This study		1:5,000
α-GFP (mouse)	Invitrogen (A11120)	AB_221568	1:500
α-GFP (chicken)	Invitrogen (A10262)	AB_2534023	1:1,000
α-RFP (rabbit)	Invitrogen (R10367)	AB_10563941	1: 2,000
α-β-galactosidase (rabbit)	Invitrogen (A11132)	AB_221539	1:500
α-β-galactosidase (mouse)	Invitrogen (MA5-15222)	AB_10980770	1:500
α-mCherry (rat)	Invitrogen (M11217)	AB_2536611	1:1,000
α-mCherry (rabbit)	Invitrogen (PA534974)	AB_2552323	1:1,000
α-DCP-1 (rabbit)	Cell signaling technology (9578)	AB_2721060	1:200
α-Crb (mouse)	DSHB (Cq4)	AB_528181	1:10
α-Rab11 (rabbit)	Andrew lab (John Hopkins University)		1:500
α-Rab7 (mouse)	DSHB (Rab7)	AB_2722471	1:10

α-Sec15 (guinea pig)	Bellen lab (Baylor College of Medicine)		1:2,000
α-α-Spectrin (mouse)	DSHB (3A9)	AB_528473	1:2
α-Discs large (mouse)	DSHB (4F3)	AB_528203	1:500
α-Pio (rabbit)	Affolter lab (Jaźwińska et al., 2003)		1:500
α-Nidogen (rabbit)	Holz lab (Wolfstetter et al., 2009)		1:2,000
α-Sulfotyrosine (mouse)	Sigma (ZMS1096-25UL)		1:50
Alexa Fluor 488/568/647-coupled secondary antibodies	Invitrogen		1:500

943

944 **References**

945 Abrams, E. W., Mihoulides, W. K., & Andrew, D. J. (2006). Fork head and Sage maintain a
946 uniform and patent salivary gland lumen through regulation of two downstream target
947 genes, PH4alphaSG1 and PH4alphaSG2. *Development*, *133*(18), 3517-3527.
948 https://doi.org/10.1242/dev.02525
949 Ahmad, M., Faiyaz Ul Haque, M., Ahmad, W., Abbas, H., Haque, S., Krakow, D., Rimoin, D.
950 L., Lachman, R. S., & Cohn, D. H. (1998). Distinct, autosomal recessive form of
951 spondyloepimetaphyseal dysplasia segregating in an inbred Pakistani kindred. *Am J Med*
952 *Genet*, *78*(5), 468-473. https://www.ncbi.nlm.nih.gov/pubmed/9714015
953 Araujo, S. J., Aslam, H., Tear, G., & Casanova, J. (2005). mummy/cystic encodes an enzyme
954 required for chitin and glycan synthesis, involved in trachea, embryonic cuticle and CNS
955 development--analysis of its role in Drosophila tracheal morphogenesis. *Dev Biol*,
956 *288*(1), 179-193. https://doi.org/10.1016/j.ydbio.2005.09.031
957 Bokel, C., Prokop, A., & Brown, N. H. (2005). Papillote and Piopio: Drosophila ZP-domain
958 proteins required for cell adhesion to the apical extracellular matrix and microtubule
959 organization. *J Cell Sci*, *118*(Pt 3), 633-642. https://doi.org/10.1242/jcs.01619
960 Bradley, P. L., & Andrew, D. J. (2001). ribbon encodes a novel BTB/POZ protein required for
961 directed cell migration in Drosophila melanogaster. *Development*, *128*(15), 3001-3015.
962 https://doi.org/10.1242/dev.128.15.3001
963 Bradley, P. L., Myat, M. M., Comeaux, C. A., & Andrew, D. J. (2003). Posterior migration of
964 the salivary gland requires an intact visceral mesoderm and integrin function. *Dev Biol*,
965 *257*(2), 249-262. https://doi.org/10.1016/s0012-1606(03)00103-9
966 Bulow, H. E., & Hobert, O. (2004). Differential sulfations and epimerization define heparan
967 sulfate specificity in nervous system development. *Neuron*, *41*(5), 723-736.
968 https://doi.org/10.1016/s0896-6273(04)00084-4
969 Chandrasekaran, V., & Beckendorf, S. K. (2003). senseless is necessary for the survival of
970 embryonic salivary glands in Drosophila. *Development*, *130*(19), 4719-4728.
971 https://doi.org/10.1242/dev.00677
972 Chu, W. C., & Hayashi, S. (2021). Mechano-chemical enforcement of tendon apical ECM into
973 nano-filaments during Drosophila flight muscle development. *Curr Biol*, *31*(7), 1366-
974 1378 e1367. https://doi.org/10.1016/j.cub.2021.01.010

975 Chung, S., & Andrew, D. J. (2014). Cadherin 99C regulates apical expansion and cell
976 rearrangement during epithelial tube elongation. *Development*, *141*(9), 1950-1960.
977 https://doi.org/10.1242/dev.104166
978 Chung, S., Hanlon, C. D., & Andrew, D. J. (2014). Building and specializing epithelial tubular
979 organs: the Drosophila salivary gland as a model system for revealing how epithelial
980 organs are specified, form and specialize. *Wiley Interdiscip Rev Dev Biol*, *3*(4), 281-300.
981 https://doi.org/10.1002/wdev.140
982 Chung, S., Kim, S., & Andrew, D. J. (2017). Uncoupling apical constriction from tissue
983 invagination. *Elife*, *6*. https://doi.org/10.7554/eLife.22235
984 Chung, S., Vining, M. S., Bradley, P. L., Chan, C. C., Wharton, K. A., Jr., & Andrew, D. J.
985 (2009). Serrano (sano) functions with the planar cell polarity genes to control tracheal
986 tube length. *PLoS Genet*, *5*(11), e1000746. https://doi.org/10.1371/journal.pgen.1000746
987 Cohen, J. D., Bermudez, J. G., Good, M. C., & Sundaram, M. V. (2020). A C. elegans Zona
988 Pellucida domain protein functions via its ZPc domain. *PLoS Genet*, *16*(11), e1009188.
989 https://doi.org/10.1371/journal.pgen.1009188
990 Cohen, J. D., Sparacio, A. P., Belfi, A. C., Forman-Rubinsky, R., Hall, D. H., Maul-Newby, H.,
991 Frand, A. R., & Sundaram, M. V. (2020). A multi-layered and dynamic apical
992 extracellular matrix shapes the vulva lumen in Caenorhabditis elegans. *Elife*, *9*.
993 https://doi.org/10.7554/eLife.57874
994 Devine, W. P., Lubarsky, B., Shaw, K., Luschnig, S., Messina, L., & Krasnow, M. A. (2005).
995 Requirement for chitin biosynthesis in epithelial tube morphogenesis. *Proc Natl Acad Sci*
996 *U S A*, *102*(47), 17014-17019. https://doi.org/10.1073/pnas.0506676102
997 Diaz-Balzac, C. A., Lazaro-Pena, M. I., Tecle, E., Gomez, N., & Bulow, H. E. (2014). Complex
998 cooperative functions of heparan sulfate proteoglycans shape nervous system
999 development in Caenorhabditis elegans. *G3 (Bethesda)*, *4*(10), 1859-1870.
1000 https://doi.org/10.1534/g3.114.012591
1001 Dierker, T., Shao, C., Haitina, T., Zaia, J., Hinas, A., & Kjellen, L. (2016). Nematodes join the
1002 family of chondroitin sulfate-synthesizing organisms: Identification of an active
1003 chondroitin sulfotransferase in Caenorhabditis elegans. *Sci Rep*, *6*, 34662.
1004 https://doi.org/10.1038/srep34662

1005 Dong, B., Miao, G., & Hayashi, S. (2014). A fat body-derived apical extracellular matrix enzyme
1006 is transported to the tracheal lumen and is required for tube morphogenesis in Drosophila.
1007 *Development*, *141*(21), 4104-4109. https://doi.org/10.1242/dev.109975
1008 Drees, L., Konigsmann, T., Jaspers, M. H. J., Pflanz, R., Riedel, D., & Schuh, R. (2019).
1009 Conserved function of the matriptase-prostasin proteolytic cascade during epithelial
1010 morphogenesis. *PLoS Genet*, *15*(1), e1007882.
1011 https://doi.org/10.1371/journal.pgen.1007882
1012 Drees, L., Schneider, S., Riedel, D., Schuh, R., & Behr, M. (2023). The proteolysis of ZP
1013 proteins is essential to control cell membrane structure and integrity of developing
1014 tracheal tubes in Drosophila. *Elife*, *12*. https://doi.org/10.7554/eLife.91079
1015 Faiyaz ul Haque, M., King, L. M., Krakow, D., Cantor, R. M., Rusiniak, M. E., Swank, R. T.,
1016 Superti-Furga, A., Haque, S., Abbas, H., Ahmad, W., Ahmad, M., & Cohn, D. H. (1998).
1017 Mutations in orthologous genes in human spondyloepimetaphyseal dysplasia and the
1018 brachymorphic mouse. *Nat Genet*, *20*(2), 157-162. https://doi.org/10.1038/2458
1019 Ford-Hutchinson, A. F., Ali, Z., Seerattan, R. A., Cooper, D. M., Hallgrimsson, B., Salo, P. T., &
1020 Jirik, F. R. (2005). Degenerative knee joint disease in mice lacking 3'-phosphoadenosine
1021 5'-phosphosulfate synthetase 2 (Papss2) activity: a putative model of human PAPSS2
1022 deficiency-associated arthrosis. *Osteoarthritis Cartilage*, *13*(5), 418-425.
1023 https://doi.org/10.1016/j.joca.2004.12.011
1024 Fox, R. M., & Andrew, D. J. (2015). Changes in organelle position and epithelial architecture
1025 associated with loss of CrebA. *Biol Open*, *4*(3), 317-330.
1026 https://doi.org/10.1242/bio.201411205
1027 Fox, R. M., Vaishnavi, A., Maruyama, R., & Andrew, D. J. (2013). Organ-specific gene
1028 expression: the bHLH protein Sage provides tissue specificity to Drosophila FoxA.
1029 *Development*, *140*(10), 2160-2171. https://doi.org/10.1242/dev.092924
1030 Ghosh, N., & Treisman, J. E. (2024). Apical cell expansion maintained by Dusky-like establishes
1031 a scaffold for corneal lens morphogenesis. *Sci Adv*, *10*(34), eado4167.
1032 https://doi.org/10.1126/sciadv.ado4167
1033 Gill, H. K., Cohen, J. D., Ayala-Figueroa, J., Forman-Rubinsky, R., Poggioli, C., Bickard, K.,
1034 Parry, J. M., Pu, P., Hall, D. H., & Sundaram, M. V. (2016). Integrity of Narrow

1035 Epithelial Tubes in the C. elegans Excretory System Requires a Transient Luminal
1036 Matrix. *PLoS Genet*, *12*(8), e1006205. https://doi.org/10.1371/journal.pgen.1006205
1037 Groza, T., Gomez, F. L., Mashhadi, H. H., Munoz-Fuentes, V., Gunes, O., Wilson, R., Cacheiro,
1038 P., Frost, A., Keskivali-Bond, P., Vardal, B., McCoy, A., Cheng, T. K., Santos, L., Wells,
1039 S., Smedley, D., Mallon, A. M., & Parkinson, H. (2023). The International Mouse
1040 Phenotyping Consortium: comprehensive knockout phenotyping underpinning the study
1041 of human disease. *Nucleic Acids Res*, *51*(D1), D1038-D1045.
1042 https://doi.org/10.1093/nar/gkac972
1043 Gunal, S., Hardman, R., Kopriva, S., & Mueller, J. W. (2019). Sulfation pathways from red to
1044 green. *J Biol Chem*, *294*(33), 12293-12312. https://doi.org/10.1074/jbc.REV119.007422
1045 Gyoergy, A., Roblek, M., Ratheesh, A., Valoskova, K., Belyaeva, V., Wachner, S.,
1046 Matsubayashi, Y., Sanchez-Sanchez, B. J., Stramer, B., & Siekhaus, D. E. (2018). Tools
1047 Allowing Independent Visualization and Genetic Manipulation of Drosophila
1048 melanogaster Macrophages and Surrounding Tissues. *G3 (Bethesda)*, *8*(3), 845-857.
1049 https://doi.org/10.1534/g3.117.300452
1050 Herman, T., & Horvitz, H. R. (1999). Three proteins involved in Caenorhabditis elegans vulval
1051 invagination are similar to components of a glycosylation pathway. *Proc Natl Acad Sci U*
1052 *S A*, *96*(3), 974-979. https://doi.org/10.1073/pnas.96.3.974
1053 Hwang, H. Y., Olson, S. K., Brown, J. R., Esko, J. D., & Horvitz, H. R. (2003). The
1054 Caenorhabditis elegans genes sqv-2 and sqv-6, which are required for vulval
1055 morphogenesis, encode glycosaminoglycan galactosyltransferase II and
1056 xylosyltransferase. *J Biol Chem*, *278*(14), 11735-11738.
1057 https://doi.org/10.1074/jbc.C200518200
1058 Ismat, A., Cheshire, A. M., & Andrew, D. J. (2013). The secreted AdamTS-A metalloprotease is
1059 required for collective cell migration. *Development*, *140*(9), 1981-1993.
1060 https://doi.org/10.1242/dev.087908
1061 Jazwinska, A., & Affolter, M. (2004). A family of genes encoding zona pellucida (ZP) domain
1062 proteins is expressed in various epithelial tissues during Drosophila embryogenesis. *Gene*
1063 *Expr Patterns*, *4*(4), 413-421. https://doi.org/10.1016/j.modgep.2004.01.003

1064 Jazwinska, A., Ribeiro, C., & Affolter, M. (2003). Epithelial tube morphogenesis during
1065 Drosophila tracheal development requires Piopio, a luminal ZP protein. *Nat Cell Biol*,
1066 *5*(10), 895-901. https://doi.org/10.1038/ncb1049
1067 Jovine, L., Darie, C. C., Litscher, E. S., & Wassarman, P. M. (2005). Zona pellucida domain
1068 proteins. *Annu Rev Biochem*, *74*, 83-114.
1069 https://doi.org/10.1146/annurev.biochem.74.082803.133039
1070 Jovine, L., Qi, H., Williams, Z., Litscher, E., & Wassarman, P. M. (2002). The ZP domain is a
1071 conserved module for polymerization of extracellular proteins. *Nat Cell Biol*, *4*(6), 457-
1072 461. https://doi.org/10.1038/ncb802
1073 Jullien, D., Crozatier, M., & Kas, E. (1997). cDNA sequence and expression pattern of the
1074 Drosophila melanogaster PAPS synthetase gene: a new salivary gland marker. *Mech Dev*,
1075 *68*(1-2), 179-186. https://doi.org/10.1016/s0925-4773(97)00136-6
1076 Kamiyama, S., Suda, T., Ueda, R., Suzuki, M., Okubo, R., Kikuchi, N., Chiba, Y., Goto, S.,
1077 Toyoda, H., Saigo, K., Watanabe, M., Narimatsu, H., Jigami, Y., & Nishihara, S. (2003).
1078 Molecular cloning and identification of 3'-phosphoadenosine 5'-phosphosulfate
1079 transporter. *J Biol Chem*, *278*(28), 25958-25963.
1080 https://doi.org/10.1074/jbc.M302439200
1081 Karlsson, M., Zhang, C., Mear, L., Zhong, W., Digre, A., Katona, B., Sjostedt, E., Butler, L.,
1082 Odeberg, J., Dusart, P., Edfors, F., Oksvold, P., von Feilitzen, K., Zwahlen, M., Arif, M.,
1083 Altay, O., Li, X., Ozcan, M., Mardinoglu, A.,…Lindskog, C. (2021). A single-cell type
1084 transcriptomics map of human tissues. *Sci Adv*, *7*(31).
1085 https://doi.org/10.1126/sciadv.abh2169
1086 Kinnunen, T., Huang, Z., Townsend, J., Gatdula, M. M., Brown, J. R., Esko, J. D., & Turnbull, J.
1087 E. (2005). Heparan 2-O-sulfotransferase, hst-2, is essential for normal cell migration in
1088 Caenorhabditis elegans. *Proc Natl Acad Sci U S A*, *102*(5), 1507-1512.
1089 https://doi.org/10.1073/pnas.0401591102
1090 Kondylis, V., & Rabouille, C. (2009). The Golgi apparatus: lessons from Drosophila. *FEBS Lett*,
1091 *583*(23), 3827-3838. https://doi.org/10.1016/j.febslet.2009.09.048
1092 Kurima, K., Warman, M. L., Krishnan, S., Domowicz, M., Krueger, R. C., Jr., Deyrup, A., &
1093 Schwartz, N. B. (1998). A member of a family of sulfate-activating enzymes causes

1094 murine brachymorphism. *Proc Natl Acad Sci U S A*, *95*(15), 8681-8685.
1095 https://doi.org/10.1073/pnas.95.15.8681
1096 Le, T. P., & Chung, S. (2021). Regulation of apical constriction via microtubule- and Rab11-
1097 dependent apical transport during tissue invagination. *Mol Biol Cell*, *32*(10), 1033-1047.
1098 https://doi.org/10.1091/mbc.E21-01-0021
1099 Legan, P. K., Rau, A., Keen, J. N., & Richardson, G. P. (1997). The mouse tectorins. Modular
1100 matrix proteins of the inner ear homologous to components of the sperm-egg adhesion
1101 system. *J Biol Chem*, *272*(13), 8791-8801. https://doi.org/10.1074/jbc.272.13.8791
1102 Litscher, E. S., & Wassarman, P. M. (2020). Zona pellucida genes and proteins and human
1103 fertility. *Trends Dev Biol*, *13*, 21-33. https://www.ncbi.nlm.nih.gov/pubmed/33335361
1104 Luders, F., Segawa, H., Stein, D., Selva, E. M., Perrimon, N., Turco, S. J., & Hacker, U. (2003).
1105 Slalom encodes an adenosine 3'-phosphate 5'-phosphosulfate transporter essential for
1106 development in Drosophila. *EMBO J*, *22*(14), 3635-3644.
1107 https://doi.org/10.1093/emboj/cdg345
1108 Luschnig, S., Batz, T., Armbruster, K., & Krasnow, M. A. (2006). serpentine and vermiform
1109 encode matrix proteins with chitin binding and deacetylation domains that limit tracheal
1110 tube length in Drosophila. *Curr Biol*, *16*(2), 186-194.
1111 https://doi.org/10.1016/j.cub.2005.11.072
1112 Lye, C. M., Naylor, H. W., & Sanson, B. (2014). Subcellular localisations of the CPTI collection
1113 of YFP-tagged proteins in Drosophila embryos. *Development*, *141*(20), 4006-4017.
1114 https://doi.org/10.1242/dev.111310
1115 Matthew, J., Vishwakarma, V., Le, T. P., Agsunod, R. A., & Chung, S. (2024). Coordination of
1116 cell cycle and morphogenesis during organ formation. *Elife*, *13*.
1117 https://doi.org/10.7554/eLife.95830
1118 McAllister, K. A., Grogg, K. M., Johnson, D. W., Gallione, C. J., Baldwin, M. A., Jackson, C.
1119 E., Helmbold, E. A., Markel, D. S., McKinnon, W. C., Murrell, J., & et al. (1994).
1120 Endoglin, a TGF-beta binding protein of endothelial cells, is the gene for hereditary
1121 haemorrhagic telangiectasia type 1. *Nat Genet*, *8*(4), 345-351.
1122 https://doi.org/10.1038/ng1294-345

1123 Mei, Z., Kuzhir, P., & Godeau, G. (2024). Update on Chitin and Chitosan from Insects: Sources,
1124 Production, Characterization, and Biomedical Applications. *Biomimetics (Basel)*, *9*(5).
1125 https://doi.org/10.3390/biomimetics9050297
1126 Moussian, B., Tang, E., Tonning, A., Helms, S., Schwarz, H., Nusslein-Volhard, C., & Uv, A. E.
1127 (2006). Drosophila Knickkopf and Retroactive are needed for epithelial tube growth and
1128 cuticle differentiation through their specific requirement for chitin filament organization.
1129 *Development*, *133*(1), 163-171. https://doi.org/10.1242/dev.02177
1130 Mueller, J. W., & Shafqat, N. (2013). Adenosine-5'-phosphosulfate--a multifaceted modulator of
1131 bifunctional 3'-phospho-adenosine-5'-phosphosulfate synthases and related enzymes.
1132 *FEBS J*, *280*(13), 3050-3057. https://doi.org/10.1111/febs.12252
1133 Myat, M. M., & Andrew, D. J. (2000a). Fork head prevents apoptosis and promotes cell shape
1134 change during formation of the Drosophila salivary glands. *Development*, *127*(19), 4217-
1135 4226. https://doi.org/10.1242/dev.127.19.4217
1136 Myat, M. M., & Andrew, D. J. (2000b). Organ shape in the Drosophila salivary gland is
1137 controlled by regulated, sequential internalization of the primordia. *Development*, *127*(4),
1138 679-691. https://doi.org/10.1242/dev.127.4.679
1139 Op De Beeck, K., Vermeire, S., Rutgeerts, P., & Bossuyt, X. (2012). Antibodies to GP2, the
1140 major zymogen granule membrane glycoprotein, in inflammatory bowel diseases. *Gut*,
1141 *61*(1), 162-164; author reply 164-165. https://doi.org/10.1136/gut.2010.233148
1142 Plaza, S., Chanut-Delalande, H., Fernandes, I., Wassarman, P. M., & Payre, F. (2010). From A to
1143 Z: apical structures and zona pellucida-domain proteins. *Trends Cell Biol*, *20*(9), 524-
1144 532. https://doi.org/10.1016/j.tcb.2010.06.002
1145 Porter, K. R., & Tamm, I. (1955). Direct visualization of a mucoprotein component of urine. *J*
1146 *Biol Chem*, *212*(1), 135-140. https://www.ncbi.nlm.nih.gov/pubmed/13233216
1147 Renner, M., Bergmann, G., Krebs, I., End, C., Lyer, S., Hilberg, F., Helmke, B., Gassler, N.,
1148 Autschbach, F., Bikker, F., Strobel-Freidekind, O., Gronert-Sum, S., Benner, A., Blaich,
1149 S., Wittig, R., Hudler, M., Ligtenberg, A. J., Madsen, J., Holmskov, U.,…Mollenhauer, J.
1150 (2007). DMBT1 confers mucosal protection in vivo and a deletion variant is associated
1151 with Crohn's disease. *Gastroenterology*, *133*(5), 1499-1509.
1152 https://doi.org/10.1053/j.gastro.2007.08.007

1153 Rutherford, S. A., Goldberg, M. W., & Allen, T. D. (1997). Three-dimensional visualization of
1154 the route of protein import: the role of nuclear pore complex substructures. *Exp Cell Res*,
1155 *232*(1), 146-160. https://doi.org/10.1006/excr.1997.3487
1156 Sarkissian, T., Timmons, A., Arya, R., Abdelwahid, E., & White, K. (2014). Detecting apoptosis
1157 in Drosophila tissues and cells. *Methods*, *68*(1), 89-96.
1158 https://doi.org/10.1016/j.ymeth.2014.02.033
1159 Smith, S. J., Davidson, L. A., & Rebeiz, M. (2020). Evolutionary expansion of apical
1160 extracellular matrix is required for the elongation of cells in a novel structure. *Elife*, *9*.
1161 https://doi.org/10.7554/eLife.55965
1162 Syed, Z. A., Bouge, A. L., Byri, S., Chavoshi, T. M., Tang, E., Bouhin, H., van Dijk-Hard, I. F.,
1163 & Uv, A. (2012). A luminal glycoprotein drives dose-dependent diameter expansion of
1164 the Drosophila melanogaster hindgut tube. *PLoS Genet*, *8*(8), e1002850.
1165 https://doi.org/10.1371/journal.pgen.1002850
1166 Tang, W. J., Fernandez, J., Sohn, J. J., & Amemiya, C. T. (2015). Chitin is endogenously
1167 produced in vertebrates. *Curr Biol*, *25*(7), 897-900.
1168 https://doi.org/10.1016/j.cub.2015.01.058
1169 Tecle, E., Diaz-Balzac, C. A., & Bulow, H. E. (2013). Distinct 3-O-sulfated heparan sulfate
1170 modification patterns are required for kal-1-dependent neurite branching in a context-
1171 dependent manner in Caenorhabditis elegans. *G3 (Bethesda)*, *3*(3), 541-552.
1172 https://doi.org/10.1534/g3.112.005199
1173 Tomancak, P., Beaton, A., Weiszmann, R., Kwan, E., Shu, S., Lewis, S. E., Richards, S.,
1174 Ashburner, M., Hartenstein, V., Celniker, S. E., & Rubin, G. M. (2002). Systematic
1175 determination of patterns of gene expression during Drosophila embryogenesis. *Genome*
1176 *Biol*, *3*(12), RESEARCH0088. https://doi.org/10.1186/gb-2002-3-12-research0088
1177 Tonning, A., Hemphala, J., Tang, E., Nannmark, U., Samakovlis, C., & Uv, A. (2005). A
1178 transient luminal chitinous matrix is required to model epithelial tube diameter in the
1179 Drosophila trachea. *Dev Cell*, *9*(3), 423-430. https://doi.org/10.1016/j.devcel.2005.07.012
1180 Turnbull, J., Drummond, K., Huang, Z., Kinnunen, T., Ford-Perriss, M., Murphy, M., &
1181 Guimond, S. (2003). Heparan sulphate sulphotransferase expression in mice and
1182 Caenorhabditis elegans. *Biochem Soc Trans*, *31*(2), 343-348.
1183 https://doi.org/10.1042/bst0310343

1184 Uhlen, M., Bjorling, E., Agaton, C., Szigyarto, C. A., Amini, B., Andersen, E., Andersson, A. C.,
1185 Angelidou, P., Asplund, A., Asplund, C., Berglund, L., Bergstrom, K., Brumer, H.,
1186 Cerjan, D., Ekstrom, M., Elobeid, A., Eriksson, C., Fagerberg, L., Falk, R.,…Ponten, F.
1187 (2005). A human protein atlas for normal and cancer tissues based on antibody
1188 proteomics. *Mol Cell Proteomics*, *4*(12), 1920-1932.
1189 https://doi.org/10.1074/mcp.M500279-MCP200
1190 van den Boom, J., Heider, D., Martin, S. R., Pastore, A., & Mueller, J. W. (2012). 3'-
1191 Phosphoadenosine 5'-phosphosulfate (PAPS) synthases, naturally fragile enzymes
1192 specifically stabilized by nucleotide binding. *J Biol Chem*, *287*(21), 17645-17655.
1193 https://doi.org/10.1074/jbc.M111.325498
1194 Venkatachalam, K. V. (2003). Human 3'-phosphoadenosine 5'-phosphosulfate (PAPS) synthase:
1195 biochemistry, molecular biology and genetic deficiency. *IUBMB Life*, *55*(1), 1-11.
1196 https://doi.org/10.1080/1521654031000072148
1197 Venkatachalam, K. V., Akita, H., & Strott, C. A. (1998). Molecular cloning, expression, and
1198 characterization of human bifunctional 3'-phosphoadenosine 5'-phosphosulfate synthase
1199 and its functional domains. *J Biol Chem*, *273*(30), 19311-19320.
1200 https://doi.org/10.1074/jbc.273.30.19311
1201 Wang, S., Jayaram, S. A., Hemphala, J., Senti, K. A., Tsarouhas, V., Jin, H., & Samakovlis, C.
1202 (2006). Septate-junction-dependent luminal deposition of chitin deacetylases restricts
1203 tube elongation in the Drosophila trachea. *Curr Biol*, *16*(2), 180-185.
1204 https://doi.org/10.1016/j.cub.2005.11.074
1205 Weiszmann, R., Hammonds, A. S., & Celniker, S. E. (2009). Determination of gene expression
1206 patterns using high-throughput RNA in situ hybridization to whole-mount Drosophila
1207 embryos. *Nat Protoc*, *4*(5), 605-618. https://doi.org/10.1038/nprot.2009.55
1208 Wilkin, M. B., Becker, M. N., Mulvey, D., Phan, I., Chao, A., Cooper, K., Chung, H. J.,
1209 Campbell, I. D., Baron, M., & MacIntyre, R. (2000). Drosophila dumpy is a gigantic
1210 extracellular protein required to maintain tension at epidermal-cuticle attachment sites.
1211 *Curr Biol*, *10*(10), 559-567. https://doi.org/10.1016/s0960-9822(00)00482-6
1212 Wolfstetter, G., & Holz, A. (2012). The role of LamininB2 (LanB2) during mesoderm
1213 differentiation in Drosophila. *Cell Mol Life Sci*, *69*(2), 267-282.
1214 https://doi.org/10.1007/s00018-011-0652-3

1215 Wong, S. H., Hamel, L., Chevalier, S., & Philip, A. (2000). Endoglin expression on human
1216 microvascular endothelial cells association with betaglycan and formation of higher order
1217 complexes with TGF-beta signalling receptors. *Eur J Biochem*, *267*(17), 5550-5560.
1218 https://doi.org/10.1046/j.1432-1327.2000.01621.x
1219 Xia, B., Royall, J. A., Damera, G., Sachdev, G. P., & Cummings, R. D. (2005). Altered O-
1220 glycosylation and sulfation of airway mucins associated with cystic fibrosis.
1221 *Glycobiology*, *15*(8), 747-775. https://doi.org/10.1093/glycob/cwi061
1222 Yan, B., Zhang, Z. Z., Huang, L. Y., Shen, H. L., & Han, Z. G. (2012). OIT3 deficiency impairs
1223 uric acid reabsorption in renal tubule. *FEBS Lett*, *586*(6), 760-765.
1224 https://doi.org/10.1016/j.febslet.2012.01.038
1225 Yang, K., Liu, M., Feng, Z., Rojas, M., Zhou, L., Ke, H., & Pastor-Pareja, J. C. (2021). ER exit
1226 sites in Drosophila display abundant ER-Golgi vesicles and pearled tubes but no
1227 megacarriers. *Cell Rep*, *36*(11), 109707. https://doi.org/10.1016/j.celrep.2021.109707
1228 Zhang, L., Song, W., Li, T., Mu, Y., Zhang, P., Hu, J., Lin, H., Zhang, J., Gao, H., & Zhang, L.
1229 (2023). Redox switching mechanism of the adenosine 5'-phosphosulfate kinase domain
1230 (APSK2) of human PAPS synthase 2. *Structure*, *31*(7), 826-835 e823.
1231 https://doi.org/10.1016/j.str.2023.04.012
1232 Zhang, P., Zhang, L., Hou, Z., Lin, H., Gao, H., & Zhang, L. (2022). Structural basis for the
1233 substrate recognition mechanism of ATP-sulfurylase domain of human PAPS synthase 2.
1234 *Biochem Biophys Res Commun*, *586*, 1-7. https://doi.org/10.1016/j.bbrc.2021.11.062
1235 Zhang, Y., Foster, J. M., Nelson, L. S., Ma, D., & Carlow, C. K. (2005). The chitin synthase
1236 genes chs-1 and chs-2 are essential for C. elegans development and responsible for chitin
1237 deposition in the eggshell and pharynx, respectively. *Dev Biol*, *285*(2), 330-339.
1238 https://doi.org/10.1016/j.ydbio.2005.06.037
1239 Zhou, W., Chang, J., Wang, X., Savelieff, M. G., Zhao, Y., Ke, S., & Ye, B. (2014). GM130 is
1240 required for compartmental organization of dendritic golgi outposts. *Curr Biol*, *24*(11),
1241 1227-1233. https://doi.org/10.1016/j.cub.2014.04.008
1242 Zhu, X., Sen, J., Stevens, L., Goltz, J. S., & Stein, D. (2005). Drosophila pipe protein activity in
1243 the ovary and the embryonic salivary gland does not require heparan sulfate
1244 glycosaminoglycans. *Development*, *132*(17), 3813-3822.
1245 https://doi.org/10.1242/dev.01962

Figure 1

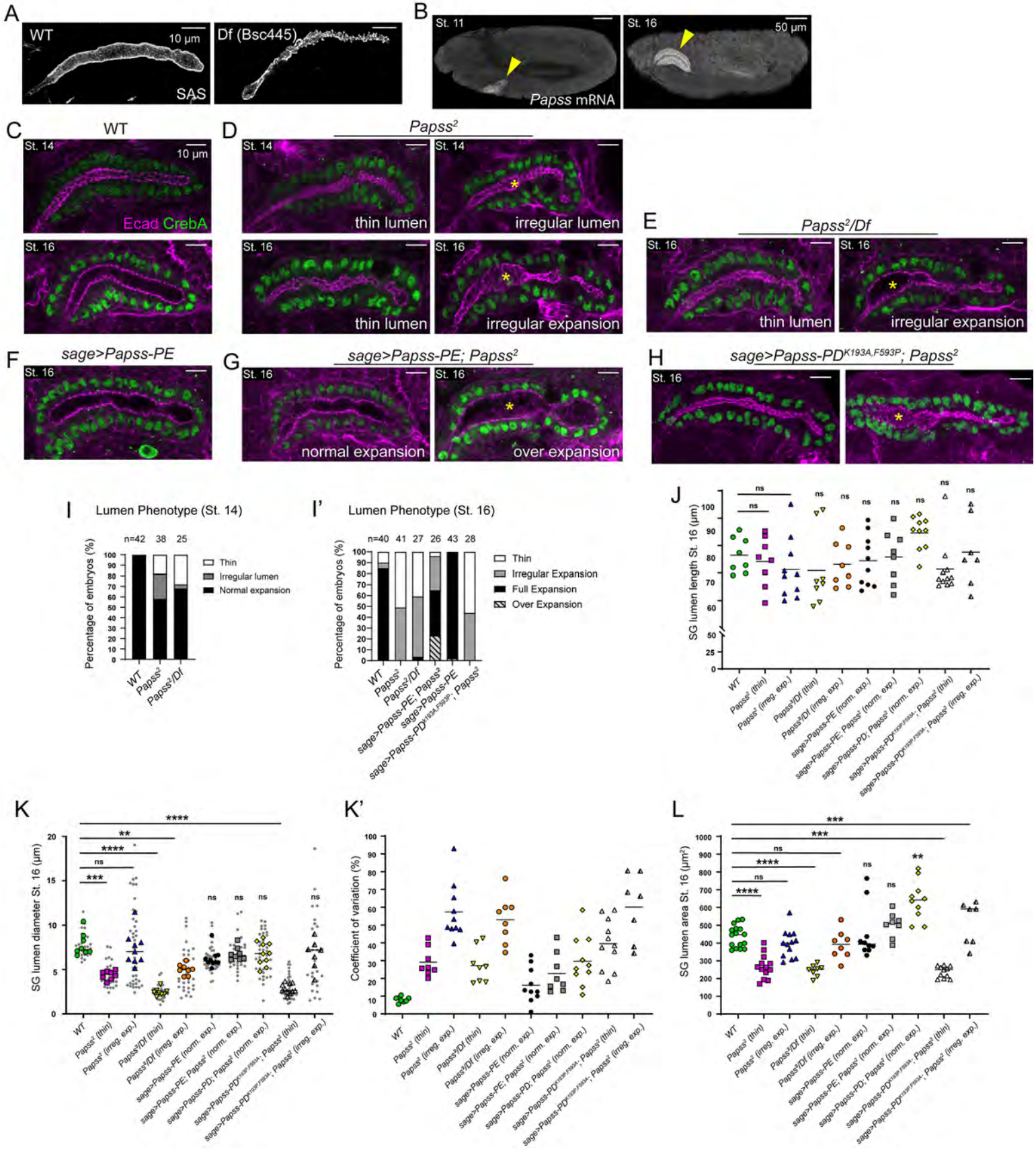
A
WT
10 µm
SAS
Df (Bsc445)
B
St. 11
St. 16
50 µm
Papss mRNA
C
WT
St. 14
10 µm
Ecad CrebA
St. 16
D
Papss2
St. 14
thin lumen
irregular lumen
St. 16
thin lumen
irregular expansion
E
Papss2/Df
St. 16
thin lumen
irregular expansion
F
sage>Papss-PE
St. 16
G
sage>Papss-PE; Papss2
St. 16
normal expansion
over expansion
H
sage>Papss-PDK193A,F593P; Papss2
St. 16
I
Lumen Phenotype (St. 14)
n=42 38 25
Percentage of embryos (%)
Thin
Irregular lumen
Normal expansion
WT
Papss2
Papss2/Df
I'
Lumen Phenotype (St. 16)
n=40 41 27 26 43 28
Percentage of embryos (%)
Thin
Irregular Expansion
Full Expansion
Over Expansion
WT
Papss2
Papss2/Df
sage>Papss-PE; Papss2
sage>Papss-PE
sage>Papss-PDK193A,F593P; Papss2
J
SG lumen length St. 16 (µm)
ns
WT
Papss2 (thin)
Papss2 (irreg. exp.)
Papss2/Df (thin)
Papss2/Df (irreg. exp.)
sage>Papss-PE (norm. exp.)
sage>Papss-PE; Papss2 (norm. exp.)
sage>Papss-PD; Papss2 (norm. exp.)
sage>Papss-PDK193A,F593P; Papss2 (thin)
sage>Papss-PDK193A,F593P; Papss2 (irreg. exp.)
K
SG lumen diameter St. 16 (µm)
****
**
****
ns
***
ns
ns
ns
ns
K'
Coefficient of variation (%)
L
SG lumen area St. 16 (µm2)
***
***
ns
****
ns
****
ns
ns
**

Figure 2

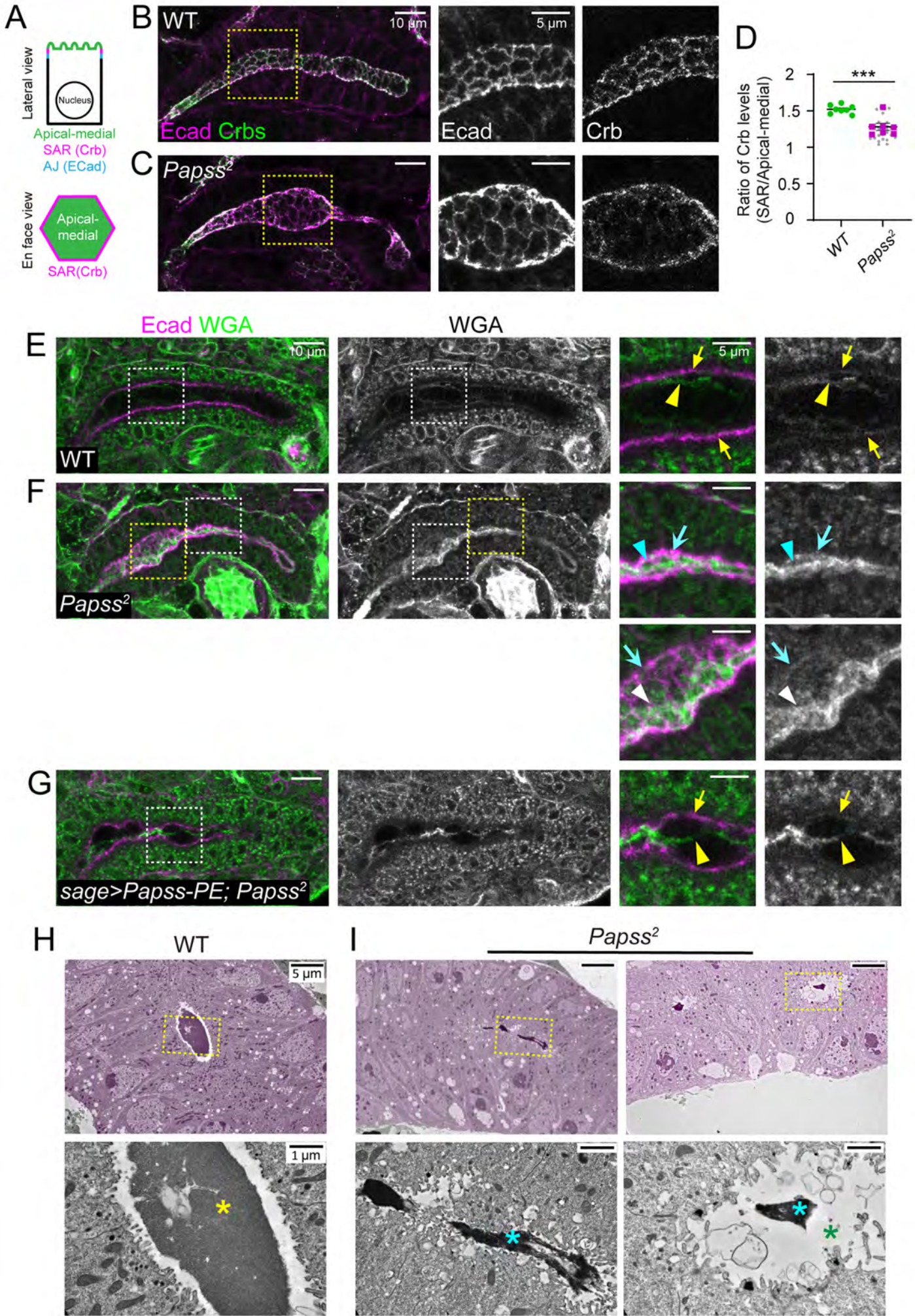
A
Lateral view
Nucleus
Apical-medial
SAR (Crb)
AJ (ECad)
En face view
Apical-medial
SAR(Crb)
B
WT
10 µm
5 µm
Ecad Crbs
Ecad
Crb
C
Papss2
D
***
Ratio of Crb levels (SAR/Apical-medial)
2
1.5
1
0.5
0
WT
Papss2
Ecad WGA
WGA
E
10 µm
5 µm
WT
F
Papss2
G
sage>Papss-PE; Papss2
H
WT
5 µm
1 µm
I
Papss2

Figure 3

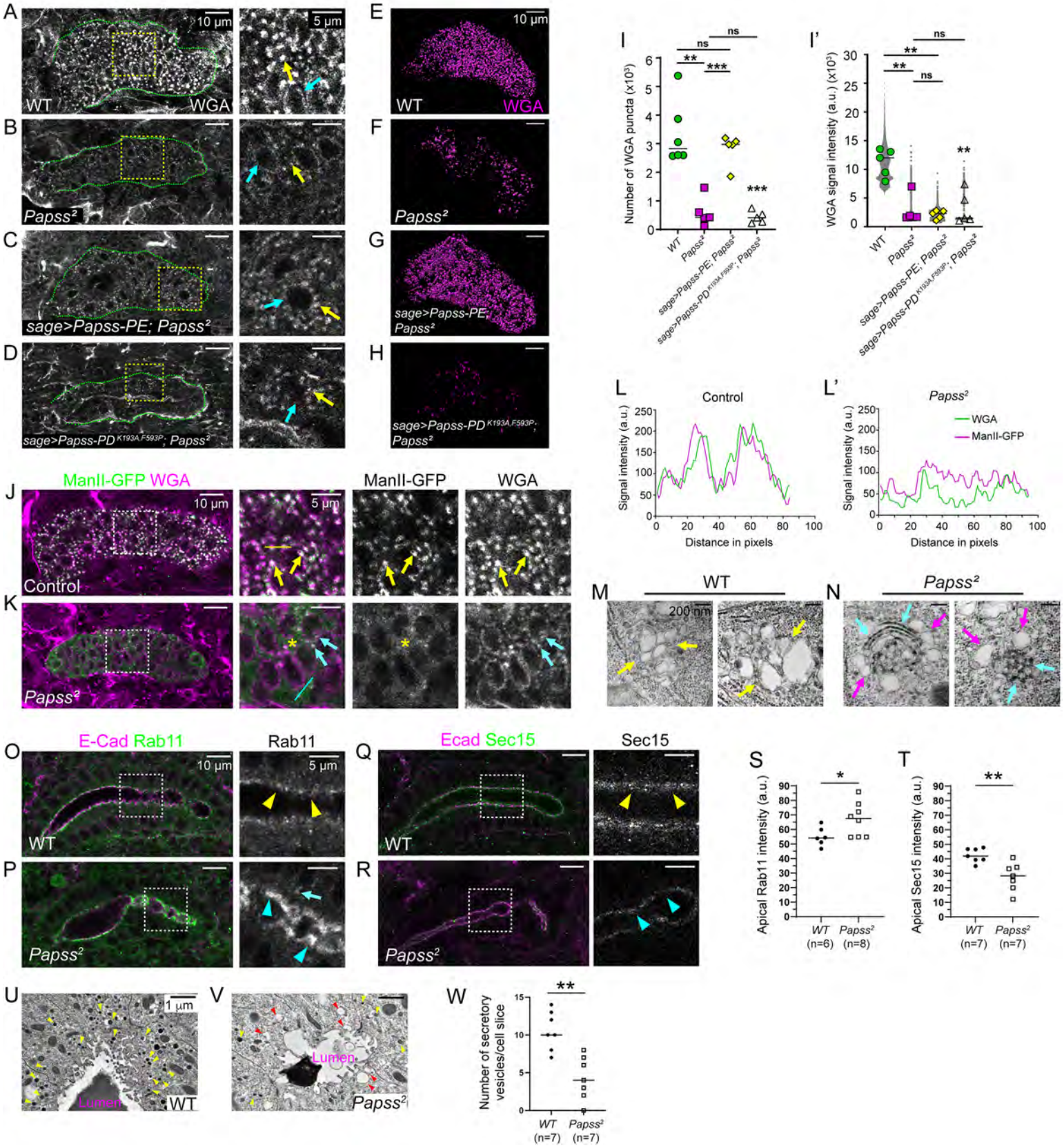
A
10 µm
5 µm
WT
WGA
B
Papss²
C
sage>Papss-PE; Papss²
D
sage>Papss-PD K193A,F593P; Papss²
E
10 µm
WT
WGA
F
Papss²
G
sage>Papss-PE; Papss²
H
sage>Papss-PD K193A,F593P; Papss²
I
Number of WGA puncta (x10³)
ns
**
***
WT
Papss²
sage>Papss-PE; Papss²
sage>Papss-PD K193A,F593P; Papss²
I'
WGA signal intensity (a.u.) (x10³)
L
Control
Signal intensity (a.u.)
Distance in pixels
L'
Papss²
WGA
ManII-GFP
J
ManII-GFP WGA
ManII-GFP
WGA
Control
K
Papss²
M
WT
200 nm
N
Papss²
O
E-Cad Rab11
Rab11
WT
P
Papss²
Q
Ecad Sec15
Sec15
WT
R
Papss²
S
Apical Rab11 intensity (a.u.)
*
WT (n=6)
Papss² (n=8)
T
Apical Sec15 intensity (a.u.)
**
WT (n=7)
Papss² (n=7)
U
1 µm
Lumen
WT
V
Lumen
Papss²
W
Number of secretory vesicles/cell slice
**
WT (n=7)
Papss² (n=7)

Figure 4

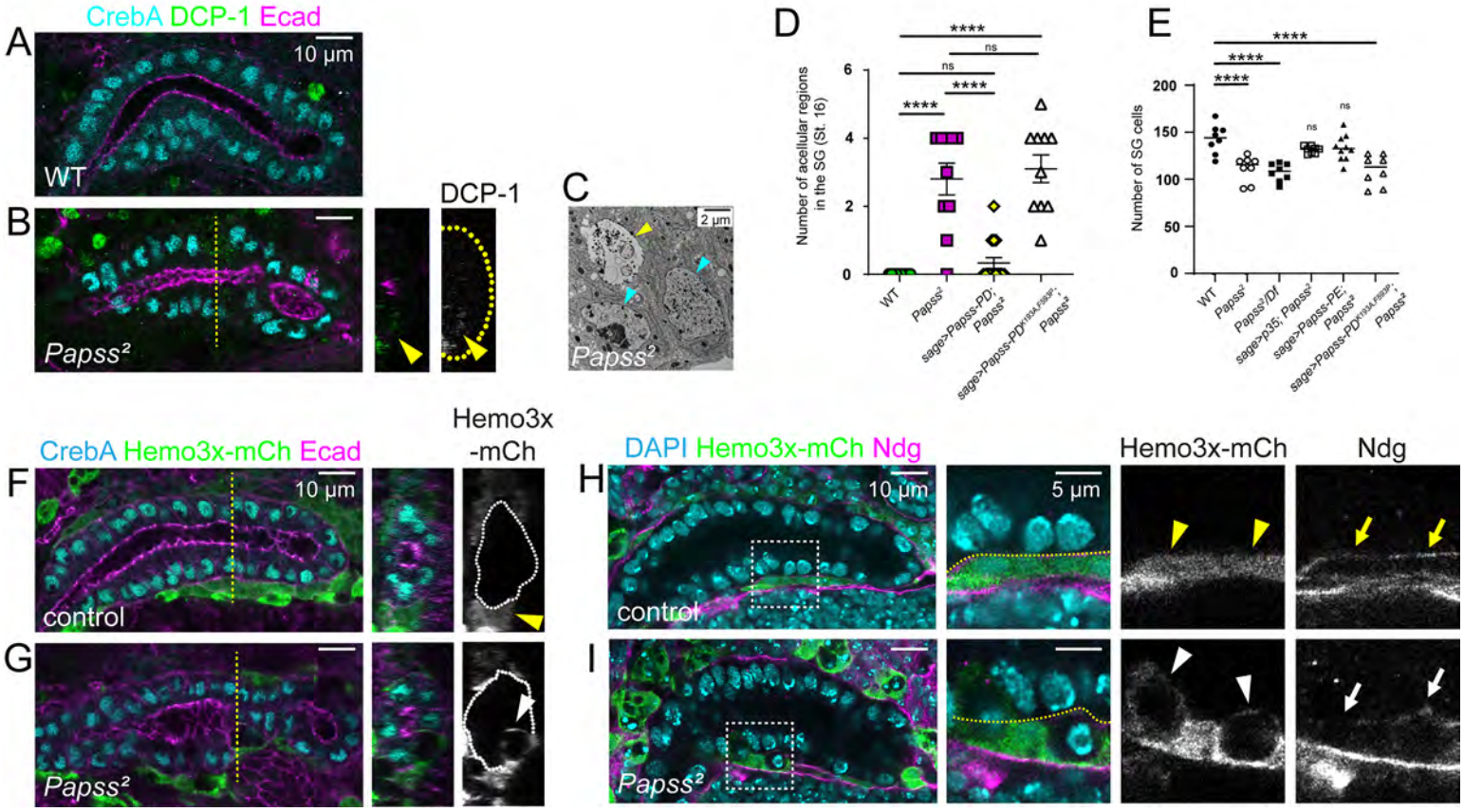
CrebA DCP-1 Ecad
A
10 µm
WT
B
Papss²
DCP-1
C
2 µm
Papss²
D
Number of acellular regions in the SG (St. 16)
****
ns
****
****
WT
Papss²
sage>Papss-PD; Papss²
sage>Papss-PD^K193A,F89P; Papss²
E
Number of SG cells
****
****
****
ns
ns
WT
Papss²
Papss²/Df
sage>p35; Papss²
sage>Papss-PE; Papss²
sage>Papss-PD^K193A,F89P; Papss²
CrebA Hemo3x-mCh Ecad
Hemo3x -mCh
F
10 µm
control
G
Papss²
DAPI Hemo3x-mCh Ndg
Hemo3x-mCh
Ndg
H
10 µm
5 µm
control
I
Papss²

Figure 5

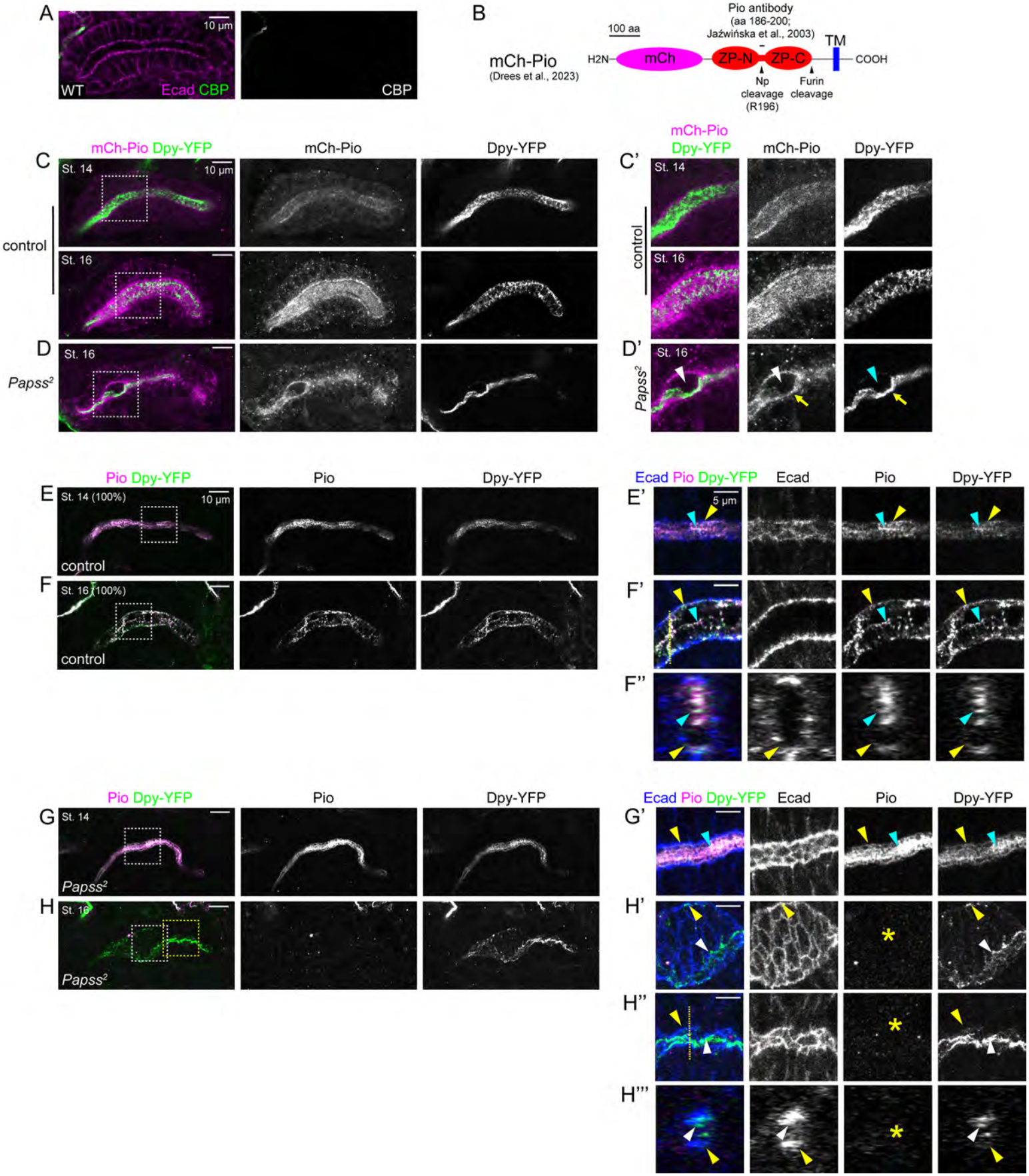
A
10 µm
WT
Ecad CBP
CBP
B
mCh-Pio
(Drees et al., 2023)
100 aa
H2N
mCh
ZP-N
ZP-C
COOH
TM
Pio antibody
(aa 186-200;
Jaźwińska et al., 2003)
Np
cleavage
(R196)
Furin
cleavage
C
mCh-Pio Dpy-YFP
mCh-Pio
Dpy-YFP
St. 14
10 µm
control
St. 16
C'
D
Papss2
D'
E
Pio Dpy-YFP
Pio
St. 14 (100%)
F
St. 16 (100%)
E'
Ecad Pio Dpy-YFP
Ecad
5 µm
F'
F''
G
St. 14
H
St. 16
G'
H'
H''
H'''

Figure 6

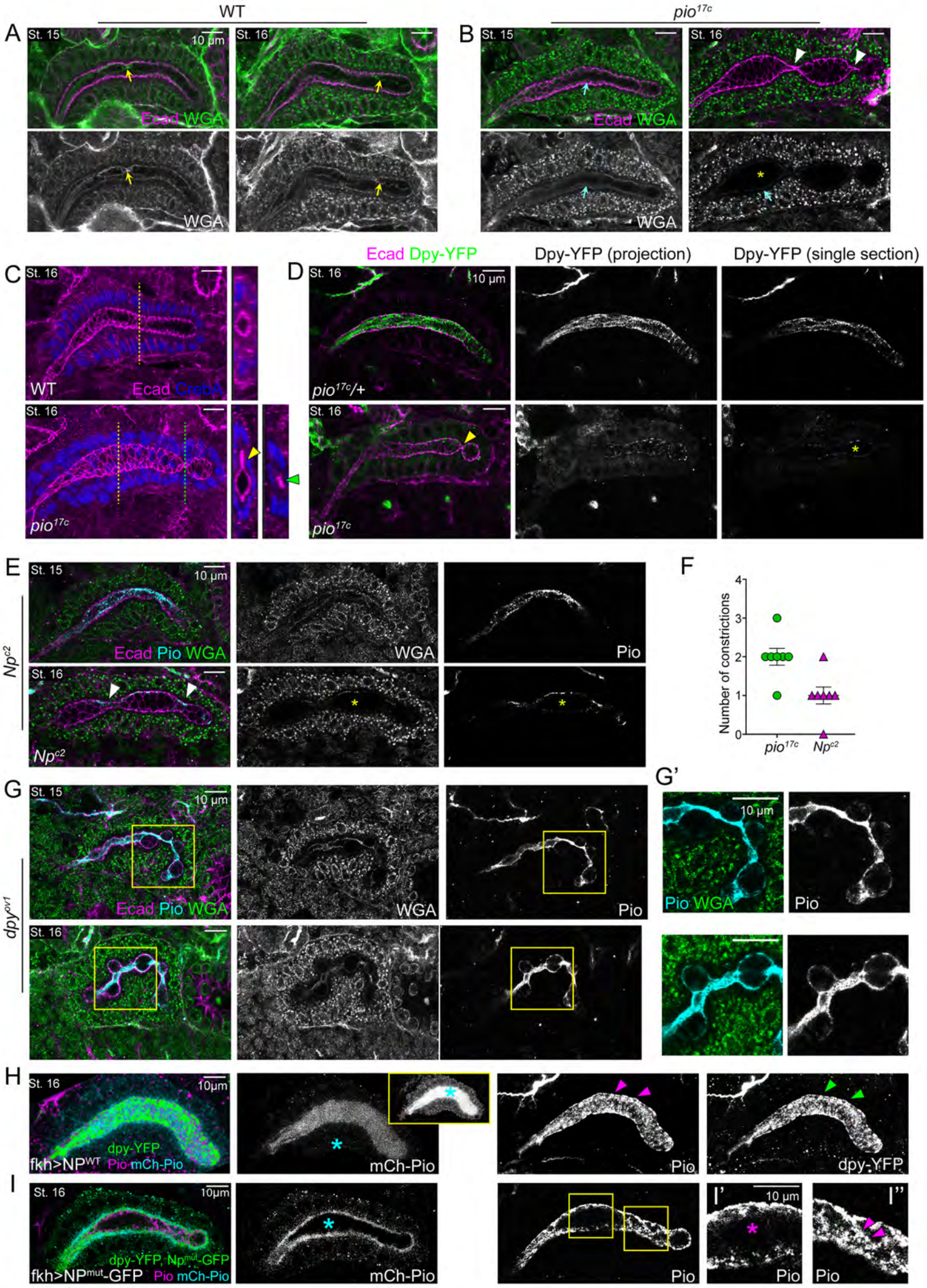
WT
pio17c
A
St. 15
St. 16
10 µm
Ecad WGA
WGA
B
C
WT
Ecad CrebA
pio17c
D
Ecad Dpy-YFP
Dpy-YFP (projection)
Dpy-YFP (single section)
pio17c/+
E
Npc2
Ecad Pio WGA
WGA
Pio
F
Number of constrictions
G
dpyov1
G'
Pio WGA
H
fkh>NPWT
dpy-YFP
Pio mCh-Pio
mCh-Pio
dpy-YFP
I
fkh>NPmut-GFP
dpy-YFP, Npmut-GFP
I'
I''

Figure 7

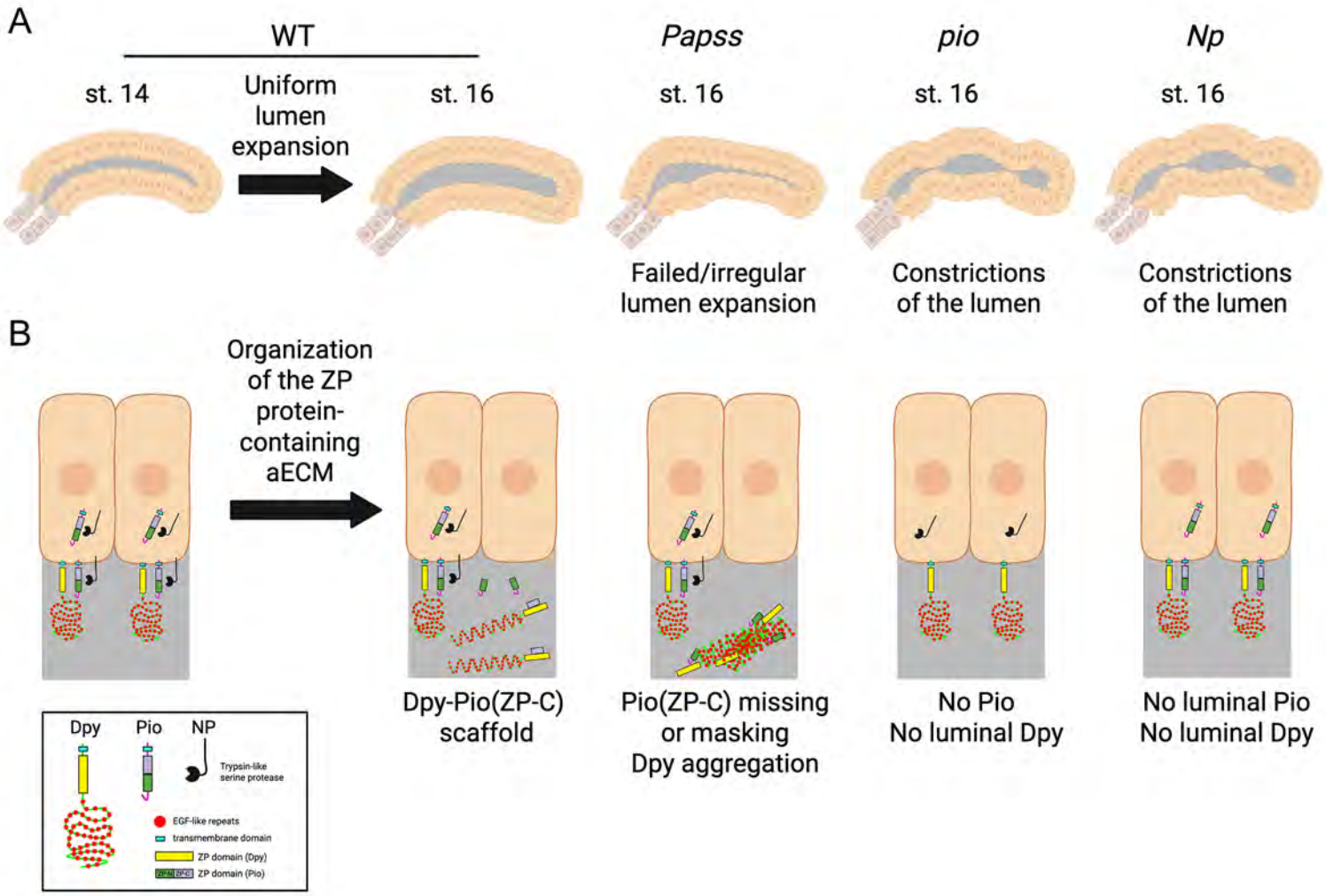
A
WT
st. 14
Uniform lumen expansion
st. 16
Papss
st. 16
Failed/irregular lumen expansion
pio
st. 16
Constrictions of the lumen
Np
st. 16
Constrictions of the lumen
B
Organization of the ZP protein-containing aECM
Dpy-Pio(ZP-C) scaffold
Pio(ZP-C) missing or masking Dpy aggregation
No Pio
No luminal Dpy
No luminal Pio
No luminal Dpy
Dpy
Pio
NP
Trypsin-like serine protease
EGF-like repeats
transmembrane domain
ZP domain (Dpy)
ZP domain (Pio)